ULF wave activity in the magnetosphere: resolving solar wind interdependencies to identify driving mechanisms

Journal of Geophysical Research: Space Physics

RESEARCH ARTICLE
10.1002/2017JA024740

Special Section:
Dayside Magnetosphere Interaction

ULF Wave Activity in the Magnetosphere: Resolving Solar Wind Interdependencies to Identify Driving Mechanisms

S. N. Bentley[1], C. E. J. Watt[1], M. J. Owens[1], and I. J. Rae[2]

[1]Department of Meteorology, University of Reading, Reading, UK, [2]Mullard Space Science Laboratory, University College London, Holmbury St Mary, UK

Key Points:
- ULF power at a single solar wind speed increases with the inclusion of parameters previously masked by solar wind interdependencies
- ULF wave power in the radiation belts can be primarily explained by solar wind speed v_{sw}, IMF $B_z < 0$, and number density perturbations deltaN_p
- These parameters suggest that the main external ULF drivers are Kelvin-Helmholtz instabilities, flux transfer events, and density pulses

Supporting Information:
- Supporting Information S1

Correspondence to:
S. N. Bentley,
s.bentley@pgr.reading.ac.uk

Citation:
Bentley, S. N., Watt, C. E. J., Owens, M. J., & Rae, I. J. (2018). ULF wave activity in the magnetosphere: Resolving solar wind interdependencies to identify driving mechanisms. *Journal of Geophysical Research: Space Physics*, *123*, 2745–2771. https://doi.org/10.1002/2017JA024740

Received 5 SEP 2017
Accepted 27 FEB 2018
Accepted article online 5 MAR 2018
Corrected 08 MAY 2018

This article was corrected on 8 MAY 2018. See the end of the full text for details.
Published online 21 APR 2018

Abstract Ultralow frequency (ULF) waves in the magnetosphere are involved in the energization and transport of radiation belt particles and are strongly driven by the external solar wind. However, the interdependency of solar wind parameters and the variety of solar wind-magnetosphere coupling processes make it difficult to distinguish the effect of individual processes and to predict magnetospheric wave power using solar wind properties. We examine 15 years of dayside ground-based measurements at a single representative frequency (2.5 mHz) and a single magnetic latitude (corresponding to $L \sim 6.6R_E$). We determine the relative contribution to ULF wave power from instantaneous nonderived solar wind parameters, accounting for their interdependencies. The most influential parameters for ground-based ULF wave power are solar wind speed v_{sw}, southward interplanetary magnetic field component $B_z < 0$, and summed power in number density perturbations δN_p. Together, the subordinate parameters B_z and δN_p still account for significant amounts of power. We suggest that these three parameters correspond to driving by the Kelvin-Helmholtz instability, formation, and/or propagation of flux transfer events and density perturbations from solar wind structures sweeping past the Earth. We anticipate that this new parameter reduction will aid comparisons of ULF generation mechanisms between magnetospheric sectors and will enable more sophisticated empirical models predicting magnetospheric ULF power using external solar wind driving parameters.

1. Introduction

Ultralow frequency (ULF) waves of frequency 1–10 mHz are implicated in the energization and the radial diffusion of electrons in the Earth's radiation belts (e.g., Elkington, 2013; Elkington et al., 1999; Fälthammar, 1965); the inward radial transport of electrons violates their third adiabatic invariant (relating to azimuthal drift) and results in an energy gain. The study of ULF waves is challenging due to the complexity of their generation mechanisms and their subsequent propagation, as established in multiple reviews of their role in magnetospheric dynamics (e.g., Mann, Murphy, et al., 2013; McPherron, 2005; Menk, 2011; Takahashi, 2016). The ability to predict power in these wave modes and hence the diffusion coefficients determining radial electron transport has long been an area of active research (Brautigam & Albert, 2000; Ozeke, Mann, Murphy, et al., 2014), in order to better predict particle populations that pose a risk to space hardware (Horne et al., 2013).

While magnetospheric ULF waves can be generated by internal sources such as plasma instabilities and substorms, ULF waves are strongly driven by coupling of the magnetosphere to the solar wind, giving rise to disturbances of the magnetopause (e.g., McPherron, 2005). These external drivers can be further categorized as either perturbations embedded in the solar wind, perturbations that originate near the bow shock or from magnetosheath instabilities, or perturbations arising at the magnetopause. For example, narrow band oscillations have been observed in both the incident solar wind pressure and the magnetospheric magnetic field (Kepko & Spence, 2003; Kim et al., 2002). Foreshock disturbances such as hot flow anomalies can create dynamic pressure perturbations, and magnetosheath pressure anisotropies can give rise to instabilities (see, e.g., Hwang & Sibeck, 2016, and references therein). The Kelvin-Helmholtz instability has long been considered a potential driver of magnetospheric ULF waves (Chen & Hasegawa, 1974), as have magnetopause perturbations such as flux transfer events (Russell & Elphic, 1979). All these mechanisms result in magnetopause perturbations that can launch fast-mode compressional waves, which then penetrate into

the magnetosphere and are then transformed and amplified by magnetospheric processes. Inward propagating fast-mode waves can become trapped between the reflecting boundaries of the magnetopause and an inner turning point such as the plasmapause (Kivelson et al., 1984; Kivelson & Southwood, 1986). Any fast-mode compressional ULF waves that reach a region where the length of the magnetic field line supports waves of a similar frequency can couple with the field line and drive standing Alfvén toroidal modes (e.g,. Obayashi & Jacobs, 1958; Radoski, 1966). Magnetic field perturbations observed at ground-based magnetometer stations are integrated over a large area of the ionosphere and will have mixed components of these standing Alfvén waves and of fast-mode compressional waves. At higher latitudes, observations of magnetic field perturbations at ground level can be used with some success to estimate the equatorial electric field (Ozeke et al., 2009; Rae et al., 2012) and hence estimate electron radial diffusion coefficients (Ozeke et al., 2012; Ozeke, Mann, Murphy, et al., 2014).

While in situ measurements of ULF waves can be made by spacecraft, ground-based stations lend themselves particularly well to long-term statistical studies of ULF waves such as those discussed below. In this paper we will use observations from a ground-based magnetometer to characterize ULF power by incoming solar wind conditions and identify the mechanisms they represent. By "ULF waves" we mean the mix of Alfvén and compressional waves detected by ground-based magnetometers in the 1 – 10 mHz range. All these wave modes are implicated in wave-particle interactions in the magnetosphere (Claudepierre et al., 2013; Degeling et al., 2008; Elkington et al., 1999, 2003; Mann, Lee, et al., 2013; Ozeke, Mann, Turner, et al., 2014; Zong et al., 2007).

While we also aim to identify physical driving mechanisms, one of the goals of this study is to set a foundation for future models and analysis of ULF wave power parameterized by solar wind properties. For such a model we would ideally have a minimal set of input parameters that are (a) ULF effective, (b) have a clear physical interpretation, and (c) are orthogonal. We do not expect to satisfy all these requirements but begin by examining the relationship between ULF power and all nonderived parameters as a compromise between inputs that are maximally physically representative and minimally interdependent. "Nonderived" quantities are defined as not explicitly dependent on other observed quantities; for example, in the OMNI data solar wind dynamic pressure P_{dyn} is calculated using velocity v_{sw} and proton number density N_p and hence is highly correlated with them. In this work we parameterize ULF wave power using the incoming solar wind properties and use the results to study ULF wave drivers. We account for solar wind interdependencies and attempt to rank the parameters and mechanisms by their effect on ULF waves.

Solar wind velocity has been strongly implicated in the generation of ULF waves; Mathie and Mann (2001) showed that to first order, ULF power can be estimated from solar wind velocity v_{sw} using an L-shell-dependent power law, and Pahud et al. (2009) showed that the magnetic local time (MLT) dependence of ULF wave power on v_{sw} varied with radial distance, or L-shell (McIlwain, 1961). Other studies have attempted to include other solar wind properties, as advocated by Engebretson et al. (1998). These investigations, examining the contribution of individual solar wind parameters, have been performed using both satellite and ground-based measurements of ULF waves as reviewed below. Satellite-based studies find that a combination of solar wind dynamic pressure, pressure fluctuations, and velocity dominates observed power. Using in situ magnetic fields at geosynchronous orbit, Takahashi and Ukhorskiy (2007, 2008) found a predominant dependence on pressure and pressure variation, while Berube et al. (2014) found that ULF wave power correlates primarily with v_{sw} outside of $L \sim 6$ and variations of solar wind dynamic pressure P_{dyn} inside. Similarly, Liu et al. (2010) found an overall dependence on pressure and pressure variations using magnetic field data but a v_{sw} dependence using electric field data, suggesting we may expect different results based on our methods of measuring ULF waves. Ground-based ULF studies find that power depends on v_{sw} across a range of L-shells (Mathie & Mann, 2001; Pahud et al., 2009; Simms et al., 2010) and Takahashi et al. (2012) found that control switches from v_{sw} to pressure variation at $L \sim 5$. The diversity of results indicate that we need to consider a systematic approach.

The importance of considering solar wind parameter interdependencies is well known; different solar wind parameters covary and thus noncausal correlations with ULF wave power exist. However, these interdependencies are difficult to account for. Some work has been done in this area, for example, Wolfe (1980) identified solar wind velocity v_{sw} as the dominant driving parameter using a stepwise multiple regression but recognized that the identification of secondary parameters was restricted by the difficulty in deconvolving the effect of nonlinear interdependencies on their relatively small data set. More recently, Simms et al. (2010) found that v_{sw}

and B_z contribute to a ULF wave index directly and that *Dst* and variations in number density and interplanetary magnetic field (IMF) contribute indirectly. They used path analysis to account for linear, exponential, and power law relationships between likely contributing parameters. Indeed, most statistical tools for disentangling such relationships assume that they are linear or require a predetermined model. Instead, in this paper we begin with a "naíve" approach, where we assume nothing about the solar wind parameter interdependencies. We systematically consider all parameters as possible ULF wave drivers to exclude those that do not contribute to magnetospheric ULF wave power and therefore identify those parameters that do. This straightforward but comprehensive approach allows us to control our assumptions carefully and determine which parameters are related to increased ULF wave power without the need to assume linear interdependencies between parameters. The background for this approach is developed in section 3. In section 4 we iteratively compare solar wind parameters to find the dominant parameters contributing to ULF wave power and, by accounting for their interdependencies, any secondary drivers which are masked by their relationship with the dominant parameters. In section 5 we review current theories of external ULF generation mechanisms and hypothesize which ones are represented by our results from section 4. The applicability of our conclusions is discussed in section 6.

2. Data

Solar wind observations are extracted from National Aeronautics and Space Administration/Goddard Space Flight Center's OMNI data set through OMNIWeb at http://omniweb.gsfc.nasa.gov/, which has already been propagated to the Earth's bow shock from the measurements near Lagrangian point L1. We exclusively use the geocentric solar magnetospheric (GSM) coordinate system (Hapgood, 1992). From the OMNI data, we use proton number density N_p, speed v_{sw}, proton temperature T, and magnetic field B with components B_z, B_x, and B_y, along with the variability of each of these parameters as calculated in section 2.1.

To characterize magnetospheric ULF wave power, we use measurements from a ground-based magnetometer array across Canada (CANOPUS, Rostoker et al., 1995, now known as CARISMA, Mann et al., 2008) from January 1990 to December 2004. In this paper we only present results from GILL (Gillam) station, whose location over this period corresponds on average to geostationary orbit at L-shell $L \sim 6.6$. GILL was chosen as it contains the largest power out of a series of stations located along the same meridian (Rae et al., 2012). The magnetometer station provides magnetic field data at 5 s resolution, which is used to calculate the amount of energy contained in oscillations at each frequency (power spectral density, or PSD) at ground level. As described in Ozeke et al. (2009), ground-based PSD can be used to infer the poloidal and toroidal waves' equatorial electric field amplitudes at the equator, for use in simulations of the outer radiation belt (Li et al., 2016; Ozeke, Mann, Murphy, et al., 2014). In future, using multiple stations will therefore give us access to a large data set spanning multiple L-shells which can be used for modeling near-Earth space. Hence, ground-based PSD is a useful descriptor of magnetospheric power.

2.1. Data Processing

Solar wind conditions are obtained from hourly OMNI data, except for the variability δX of each solar wind parameter X, which is calculated in 1-hr intervals from the 1-min OMNI data. If there are eight minutes or fewer missing per hour, data gaps are interpolated. If there are more than 8 min of missing data per hour, the interval is discarded. Power in each hour is found by detrending and using the multitaper method (Percival & Walden, 1993; Thomson, 1982). We define the variability δX in the solar wind to be the sum of power across 1.7–6.7 mHz, which represents the power in perturbations of parameter X, a broadband solar wind source.

The ground-based magnetometer data are transformed to geomagnetic H, D, Z coordinates (north-south, east-west, and orthogonal to the surface of the Earth) using International Geomagnetic Reference Field/Definitive Geomagnetic Reference Field values for that year and station, from http://omniweb.gsfc.nasa.gov/vitmo/cgm_vitmo.html. MLTs are calculated from the same source; we use only information from 3 to 21 MLT, excluding the midnight sector to remove effects such as substorm-related ULF wave power from this region. Data time stamps are inspected to prevent double counting, any instances of which are removed. We require that absolute values of the ground magnetic field lie between 5.8 and 6.4 $\times 10^4$ nT, regarding anything outside this range as unphysical. We interpolate up to 5 min of every hour from the time series; if any more data are missing, the hour is omitted from our data set. This is more stringent than for the OMNI data, because we require better frequency resolution; we use summed power for each δX but want to consider individual frequencies in the magnetosphere. At this point corresponding solar wind

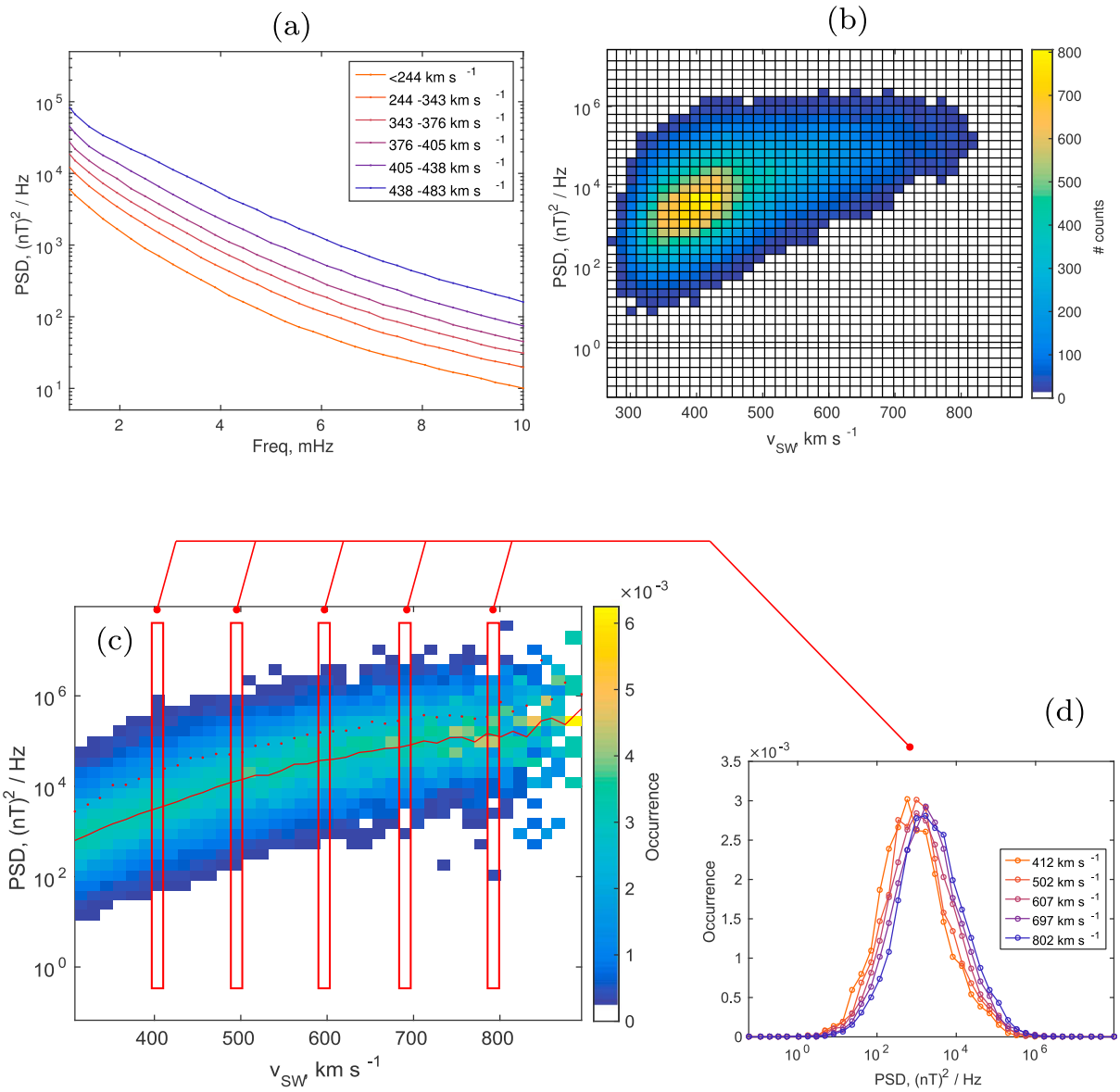

Figure 1. (a) Example median ultralow frequency wave power spectral density (PSD) for each solar wind speed sextile at GILL station across 1–10 mHz. (b) Occurrence statistics of PSD at 2.5 mHz at each solar wind speed at GILL. (c) Probability distribution functions from the occurrence statistics in (b), normalized such that the probability adds up to one in each solar wind speed bin. The red solid line indicates the median ultralow frequency wave power in each speed bin, which here follows the "peak" of the distribution, while the red dotted line is the mean, which is skewed to the high-powered tail. For each solar wind speed bin the distribution of power is roughly lognormal, as shown by the example distributions in (d), which displays some of the sample probability distribution functions in specific speed bins from (c).

properties from the same hour are assigned to the magnetometer data and we consider only hourly data that are complete in both sets. Before calculating the power spectral density from the ground magnetometer data, each hourly time series is detrended and a low-pass Butterworth filter is applied to prevent aliasing. The PSD is then estimated using the multitaper method, where several spectral estimates are constructed and averaged using orthogonal windowing functions. This provides a spectral estimate with frequency resolution 0.278 mHz. The multitaper method was chosen, as it provides a more statistically consistent estimate than a simple fast Fourier transform and it also mitigates some of the effects of cutting up our data into arbitrary hours using rectangular windows (National Semiconductor Corporation, 1980; Stoica & Moses, 2005).

Since ULF waves of frequency 1–10 mHz have periods on the order of minutes, hour-long windows are suitable to resolve the required frequency band. Using an hour window also includes time for the wave-driving

mechanisms and for wave propagation, as the estimated propagation time of compressional waves to the radiation belts is on the order of minutes (Chi et al., 2006). We assume that the magnetosphere is close to stationary on timescales of an hour. The stationarity assumption is necessary for use of the multitaper method and is reasonable given the timescale of ULF wave processes of interest. More dynamic drivers exist, such as transient ion foreshock phenomena, (see, e.g., Hartinger et al., 2013; Hwang & Sibeck, 2016). However, these cannot be easily studied using data at L1, and their transiency would require a shorter window with reduced frequency resolution.

The lower bound of our frequency range is chosen to exclude spectral leakage from 0 mHz during the PSD calculation. Figure 1 provides justification for our analysis choices in this study. In Figure 1a the median PSD value is shown for sextiles of solar wind velocity across our frequency range. Figure 1b shows the occurrence statistics of all PSD at 2.5 mHz binned by solar wind speed, which is used to create probability distribution functions for each speed bin in Figure 1c. Several examples of these distributions are extracted and shown in Figure 1d. From Figure 1a we see that power decreases smoothly with frequency and hence there is no clear upper limit and no preferred frequency within this range to study. We have chosen 10 mHz as an arbitrary cutoff point, since this includes most of the power in the system. Thus, the processed data consist of a set of solar wind conditions associated with magnetospheric power spectral densities across frequencies 1–10 mHz from four geomagnetic stations across 15 years. Despite only beginning with a single station, the number of parameters and the spatial and temporal properties require still more reduction to be manageable. In this paper we only present the results of a single frequency, 2.5 mHz, which is at the high-powered end (i.e., the low-frequency end). We will study the full frequency range in future work. We also only present the results for the geomagnetic north-south ground coordinate (H) corresponding to azimuthal fluctuations in the radiation belts. Other frequencies and the east-west coordinate (D) are examined briefly to confirm qualitatively similar results while a quantitative comparison is reserved for future work.

3. Background Analysis

In order to characterize the relation between the solar wind parameters and the observed power, it is necessary to first account for the fact that some solar wind conditions occur more often than others. Otherwise any resultant distributions or relationships we extract will be skewed. This is illustrated in the intensity maps found in Figure 1b, where we bin the occurrence of ULF wave power at a given frequency ($f = 2.5$ mHz) at a single station (GILL) by solar wind speeds. The triangle shape in Figure 1b demonstrates that our data are not evenly distributed over all solar wind speeds; for example, we have more data for a solar wind speed of 300–400 km/s than for 500–600 km/s. It is interesting to note that these distributions are very similar to the occurrence of electron flux and v_{sw} in both Reeves et al. (2011) and Figure 1 of Kellerman and Shprits (2012), especially as ULF waves are theorized to be related to electron flux (Mathie & Mann, 2000). We follow the approach in Kellerman and Shprits (2012) to calculate the probability distribution function; we normalize the observed counts of PSD in each parameter bin by the sum of counts in that bin, so that the power distribution for each parameter interval is then represented by an equal number of points and the total number of counts in each vertical slice is the same. In doing so we calculate the conditional probability of observing each power value for a given solar wind speed bin centered at v_{sw}. In Figure 1c it can be observed that the resultant distribution for solar wind speed increases smoothly and that for each vertical slice (each parameter bin) the probability distribution of power is apparently lognormal (Figure 1d).

We normalize the intensity maps of ULF wave power due to other solar wind parameters in the same way. The distribution of ULF wave power for values of each solar wind parameter—the vertical slices—also appear to be lognormal (see Figure S1 in the supporting information). Given such well-defined distributions, we consider the median PSD of each parameter bin to be the concise and representative reduction of the data set we need. Furthermore, the median is conserved (and indeed converges) with additional observations. Although the arithmetic mean is often used to describe statistical wave amplitude characteristics (e.g., Spasojevic et al., 2015), in lognormal distributions the mean is highly skewed toward the high-powered tail whereas the median is directly related to the mean of the corresponding normal distribution (Johnson et al., 1994). We therefore use the median exclusively in our analysis of ULF power. A descriptor of the spread of each distribution (such as the lognormal variance or the interquartile range) would be of additional value and will be explored in future studies.

Relationships between solar wind parameters are determined by the type of the solar wind (and hence their source) and by interactions between solar wind types as they propagate toward Earth. For example, the faster solar wind is less dense and the slow solar wind is often more variable (Geiss et al., 1995), but the faster solar wind may catch up with slower solar wind, creating areas of compression and rarefaction that make up stream interaction regions (e.g., Jian et al., 2006). In this paragraph we discuss the relationships we expect to see in our subset of the solar wind data. These are confirmed briefly here and can be found in more detail in Figures S3–S6 of the supporting information. As expected, in our data set the velocity observed near L1 is close to radial and there is an anticorrelation between proton number density and solar wind speed which is not linear. The interplanetary magnetic field displays evidence of the Parker spiral, and there is a correlation between proton temperature and flow speed. These interdependencies will need to be accounted for. In our method we should also consider relationships with perturbations δX of each parameter X. If all perturbations observed near L1 are due to some combinations of random processes, wave processes, and structures from interactions between solar wind regions, we may expect that δX contain contributions both independent from and related to the original parameter X. Therefore, we assume that δX inherits interdependencies from X, in addition to the relations between perturbations of velocity, number density, and the magnetic field from magnetohydrodynamic waves. The parameters $\delta B_{x,y,z}$ and δN_p are found in the same types of solar wind and will therefore appear to correlate with one another; in the coronal mass ejection (CME) sheath region there are lots of variability as the faster solar wind causes the preceding solar wind to bunch up, often forming planes of different magnetic field orientation which are also the situations in which we find the largest δN_p (Nakagawa et al., 1989). The interior region of CMEs exhibit other interdependencies; there is often a low proton temperature, high B_z, and low number density N_p (Owens et al., 2005). While events such as CMEs are relatively rare and so are not obvious in large statistical distributions, they are also particularly geoeffective (e.g., Plunkett & Wu, 2000) and so it is possible that they might weight parameter contributions to ULF wave power. Therefore, we must be able to account for all such interdependencies.

As electron density and temperature are not included in the OMNIWeb data set, they cannot be analyzed despite our aim to investigate all nonderived parameters. However, we are not concerned as the electron number density follows the proton number density fairly well over hour-long timescales (else, charge neutrality would not be valid in the solar wind) and electron temperature has been found to be roughly 141,000 K independent of any other solar wind characteristics (Newbury et al., 1998), and hence does not have parameter interdependencies to resolve.

Previous work (e.g., Baker et al., 2003; Cao et al., 1994; Pahud et al., 2009; Takahashi et al., 2012) has identified a clear MLT dependence of ULF wave power. The details of any MLT dependence are clearly important but are out of the scope of this work; here we aim to account for solar wind interdependencies and identify those dominant parameters that should be used to quantify MLT differences in future work. For reference, intensity maps such as in Figure 1b for each MLT sector can be found in the supporting information, Figure S2.

Before proceeding further, we note the additional implicit assumptions in this approach and examine their corresponding physical limitations. To begin with, taking multiple hour-long snapshots assumes that it makes sense to compare them—that the behavior of the magnetosphere will be similar under similar solar wind conditions and that the behavior we see is due solely to those conditions. We do not account for internal processes or for the initial state of the magnetosphere; that is, the magnetosphere has no history longer than an hour. Obviously, this is not always a good approximation but we assume that over the long time period of our analysis it adds noise rather than any systematic bias. Furthermore, by using the median we assume that the system can be described statistically and that essentially each hour-long observation is a separate run of the same "experiment" under different conditions. This assumption is supported by the existence of lognormal power distributions for each parameter. Finally, as the driving variables we are considering are interdependent we need to find a way to isolate the contribution of each and to identify the causal parameters. We consider "causal" parameters to be those parameters that correlate with magnetospheric ULF power and whose contribution cannot be attributed to their covariance with other solar wind parameters in our analysis. In particular we need to compare relative contributions between parameters since the correlation of power with solar wind speed is dominant and may be masking other secondary mechanisms. The clear dependence of ULF wave power on increasing solar wind speed is shown in Figure 1a.

Ideally, we would bin by all parameters and examine their individual contribution. However, this would result in a high-dimensional parameter space that would be difficult to analyze and would have poor data resolution.

Instead we simplify by studying only two parameters at once, which allows us to compare their relative contributions with adequate data resolution. If the first of these parameters is solar wind speed we can identify whether the second parameter has an independent contribution. Finally, bins are only used if they contain at least 10 data points.

4. Results: Determining Solar Wind Parameter Contribution to Magnetospheric ULF Wave Power

We present the parameters of interest individually. We have used observables in the solar wind that are not derived from one another; hence, we do not study electric field E or dynamic pressure P_{dyn} which are derived from $v_{sw}B$ and $N_p v_{sw}^2$, respectively. To compare the relative contribution of any two parameters to magnetospheric power, we bin all data using those two parameters and then calculate the median-observed PSD of all hours in each bin. In particular, if one of these binning parameters is solar wind speed we will have controlled for any speed-dependent relationship. The aim of this section is to explore and identify contributing parameters as outlined in the workflow diagram in Figure 2; we examine the median PSD in terms of v_{sw} and each parameter X to establish whether X contributes to power, then iteratively examine the effect from each pair of contributing parameters. These iterative comparisons turn out to be particularly necessary for N_p and $B_{x,y,z}$. A summary of the resulting main ULF-effective parameters can be found in section 4.8, while a discussion of the physical mechanisms they represent is presented in section 5.

We begin the discussion of each parameter with a summary of solar wind interdependencies confirmed in section S2 of the supporting information.

4.1. Solar Wind Velocity Components

While the solar wind velocity is expected to dominate contributions to ULF power, for our systematic approach it should be confirmed whether this contribution is contained within the bulk flow v_{sw} or within the velocity components (in GSM coordinates) v_x, v_y, or v_z. Since v_{sw} is almost entirely composed of radial flow v_x, this question becomes whether the $v_{y,z}$ contributions to magnetospheric ULF power are significant compared to that from v_x. In Figures 3a and 3b hours are binned by the solar wind v_x and v_y and v_x and v_z, respectively, where the median PSD at 2.5 mHz of those hours is shown. In Figures 3c–3f cut-throughs of the median PSD at individual bins is shown. For these cut-throughs, we hold one parameter constant and show whether, for that constant value, an increase in the second parameter (along the x axis) is associated with an increase in PSD. Therefore, any horizontal results would indicate that there is no dependence of power on that second parameter, whereas a steep gradient would indicate that PSD increases strongly with increases in that parameter. Hence, Figures 3a and 3b show that the majority of the observed ULF wave power can be attributed to v_x. While there are small possible effects due to higher absolute v_y, v_z velocities, particularly at lower v_x, ULF power is largely controlled by the v_x component. This is particularly clear from the cut-throughs shown in the side panels (c), (d) and (e), (f), where the PSD is highly ordered by v_x but shows little or no relationship with v_y or v_z.

One effect of increased v_y, v_z would be to change the geometry of the magnetosphere, for example, shifting the nose location relative to the Earth. Since this analysis is performed over observations where our ground station lies in 3–21 MLT, it is possible that if significant increases and decreases of power exist due to a shift toward dawn or dusk, they may still not appear in our statistics as they are averaged out over multiple MLT sectors. However, this nose shift is relatively small; given extreme nonradial flows in 1-hr data (e.g., $v_{NR} = 50$ km/s) primarily occur within the sheath region of fast CMEs (Owens & Cargill, 2004), they are typically accompanied by high radial velocity, for example, $v_x > 600$ km/s. Thus, the solar wind striking angle $\theta = \arctan \frac{v_{NR}}{v_x}$ is constrained below ~5° off the radial Sun-Earth line. In terms of magnetic local time coordinates, this shift of the nose corresponds to a relatively small change of ~24 min. Hence, we would expect this effect to be negligible. Given this and the two-parameter plot results in Figure 3, we therefore choose speed $v_{sw} \sim v_x$ to characterize the solar wind velocity control of magnetospheric power for ease of comparison with other studies.

4.2. Speed Perturbations δv_{sw}

Previous studies have indicated a ULF wave power dependence on speed perturbations or variability (Pokhotelov et al., 2015), but the interdependence of δv_{sw} with v_{sw} has not been fully explored. It is possible that the summed power δv_{sw} (or indeed the variance) will increase in magnitude with the speed v_{sw}, so there is an interdependence to account for. In Figure 4a we bin the observations by v_{sw} and δv_{sw} values for that hour

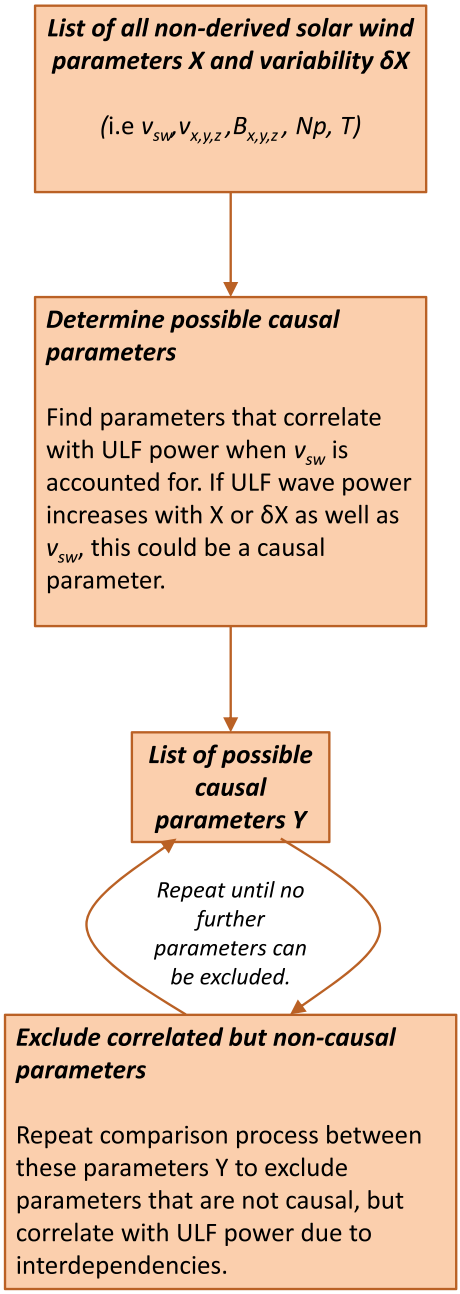

Figure 2. An overview of the method followed in this paper to systematically identify causal parameters. Beginning with a list of all nonderived solar wind parameters, we determine which could possibly be causal parameters. This is done by examining power spectral density at one frequency at one station as a function of two parameters; we bin by v_{sw} and each parameter X and δX and observe whether the median-observed ultralow frequency power spectral density correlates with X or δX for constant values of v_{sw}. Parameters that are then observed to correlate with power could be causal. Once this list of possible causal parameters is found, we can repeat this comparison process to exclude parameters that correlate due to interdependencies. For example, we remove the effect of a known existing parameter by taking a single bin such as $v_{sw} = 300-450$ km/s. Then by comparing two other parameters $Y_1 and Y_2$, we can see whether ultralow frequency wave power increases in either once the interdependency has been accounted for. They are removed from the list of possible causal parameters if not.

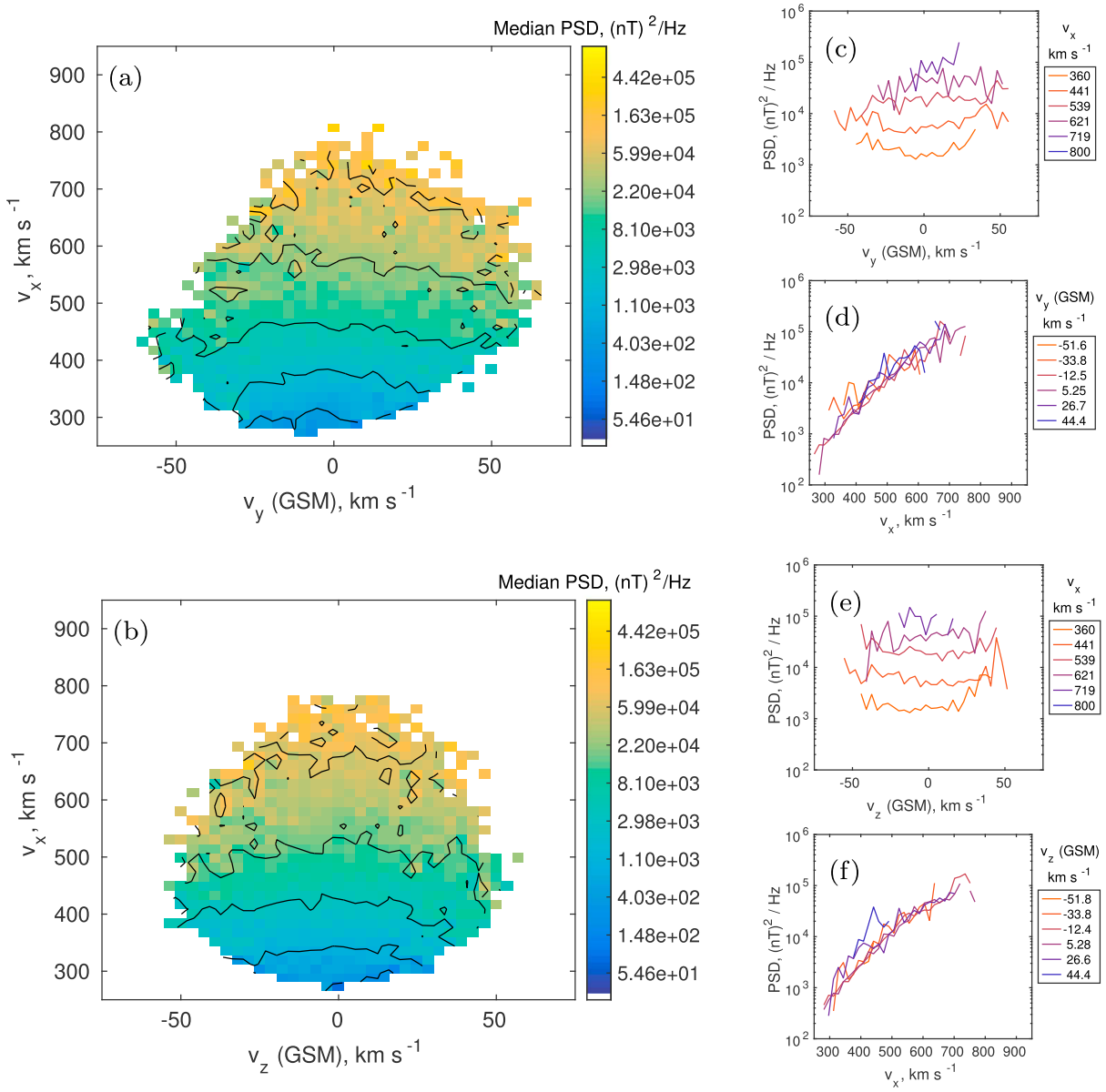

Figure 3. Data are binned using the observed value of the solar wind velocity in (a) GSM *x* and *y* and (b) GSM *x* and *z* directions for each hour. In each bin, the median power spectral density (PSD) found at 2.5 mHz at GILL is displayed. Five contours across the median PSD values are shown. (c–f) On the right, vertical and horizontal slices are taken at constant, equally spaced values to show the relationship between PSD and the individual variables.

and take the median-observed ULF power in each bin. The coverage in (v_{sw}, δv_{sw}) space indicates that δv_{sw} does increase with v_{sw}. However, magnetospheric ULF power increases only with v_{sw}, not with power δv_{sw} in the perturbations. In particular, both the horizontal and vertical cut-throughs at constant v_{sw} (Figure 4b) and constant δv_{sw} (Figure 4c) indicate a power dependence only on v_{sw}, because the cut-throughs in Figure 4b are roughly horizontal. Hence, it is likely that the relationship shown in Pokhotelov et al. (2015) is due to the interdependence between v_{sw} and δv.

4.3. Proton Number Density N_p and Perturbations δN_p

The relationship between v_{sw} and N_p or δN_p depends strongly on the type of solar wind. Generally, due to differences in the fast and slow solar wind, we can expect to observe high N_p with low v_{sw} and vice versa. In addition to any relationship between N_p and δN_p, we will expect to see higher δN_p in compression regions and in sheath regions (Owens et al., 2005) where we would also see high v_{sw} and magnetic field perturbations.

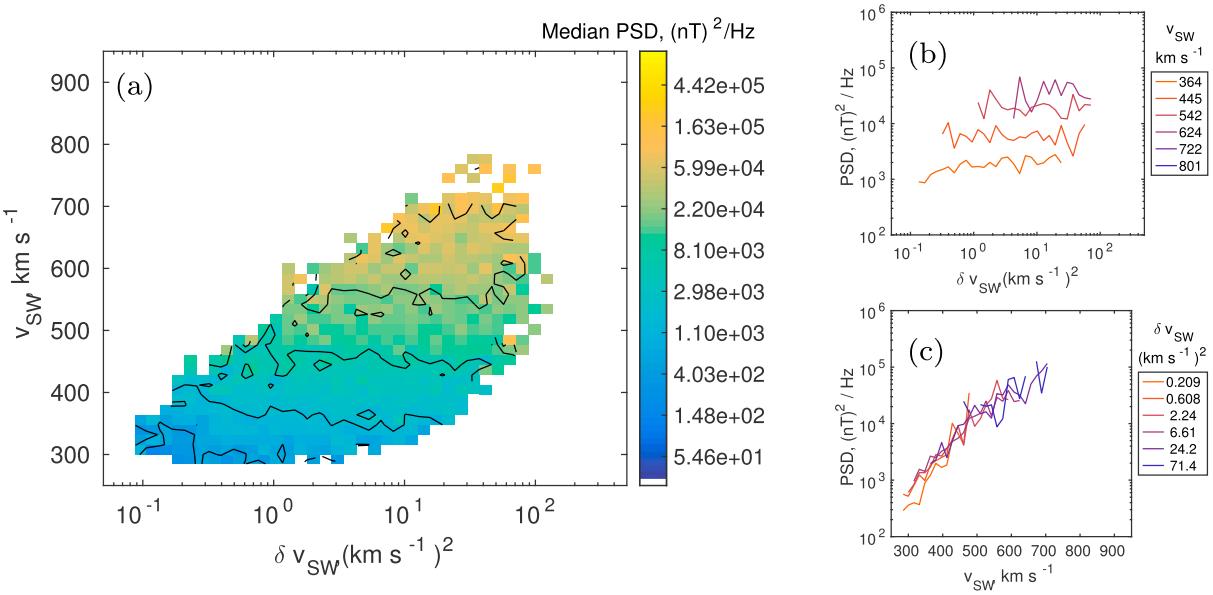

Figure 4. Same as in Figure 3, but exploring the dependence of magnetospheric ultralow frequency power on the mean solar wind speed and the power δv_{sw} in its perturbations. We bin by v_{sw} and δv_{sw} and display the median power observed in each bin at 2.5 mHz. Cut-throughs at constant v_{sw} and δv_{sw} are shown in (b) and (c), respectively. PSD = power spectral density.

In Figure 5 we examine whether N_p makes a contribution to ULF wave power independently from v_{sw}. In Figure 5a we see that power increases with v_{sw} as expected, but that it also increases with N_p. However, this also appears to be true for δN_p as shown in Figure 5c. We can suppose that there may be some relationship between δN_p and N_p and so we must see which contributes to the observed power. To exclude the dependence of N_p and δN_p on v_{sw} Figure 5b shows median ULF wave power calculated only using hours where the solar wind speed is between 300 and 450 km/s. Here we see that increases in ULF median PSD correspond to increasing δN_p and not increasing N_p. For completeness, the corresponding plot for all speeds is included in the supporting information as it illustrates the necessity of controlling the N_p - v_{sw} interdependency in the solar wind. Therefore, we conclude that δN_p, not N_p, is the more immediate contributor to power observed in magnetospheric ULF waves measured using ground-based magnetometers.

The cut-throughs in Figures 5d and 5e demonstrate this v_{sw} - δN_p dependence; in Figure 5d, purely horizontal slices would indicate a dependence solely on v_{sw}, whereas a vertical result would show that power depended only on δN_p. The angle of the constant speed slices confirm that v_{sw} is the dominant parameter. We also note that in Figure 5d the additional δN_p contribution is observed at all speeds.

4.4. IMF Components and Their Perturbations

As IMF **B** is a vector with highly interdependent components, we must first examine all components $B_{x,y,z}$ and their perturbations $\delta B_{x,y,z}$ for a correlation with PSD and then compare against each other to recognize whether each possible correlation is causal or due to intercomponent relationships. Components $B_{x,y}$ are interdependent due to the Parker spiral, while B_z is highly dependent on the type of solar wind; for example, it is often far larger in sheath regions of CMEs (Owens & Forsyth, 2013). The total field magnitude $|B|$ is higher in compressed regions of the solar wind and each δB_i inherit these dependencies plus contributions from wave activity and random processes. Therefore, we must first compare individual components $B_{x,y,z}$ to v_{sw} and, subsequently, components $\delta B_{x,y,z}$ to v_{sw}. By splitting the analysis in this way we will identify any possible causal parameters whose interdependencies we can resolve by then comparing to each other, for example, comparing each B_i and δB_i contribution, ideally while holding v_{sw} constant.

We present B_z first as it is important for studying solar wind coupling to the magnetosphere (e.g., Dungey, 1961). Figure 6a shows ULF power as a function of v_{sw} and B_z. We see that for $B_z > 0$ there is very little contribution to observed ULF power due to the magnetic field component B_z. However, there is a clear increase in power for more strongly negative B_z at any given solar wind speed. B_z clearly contributes to observed power but only below the threshold $B_z = 0$. For example, at v_{sw} ~600 km/s for $B_z > 0$ the median power

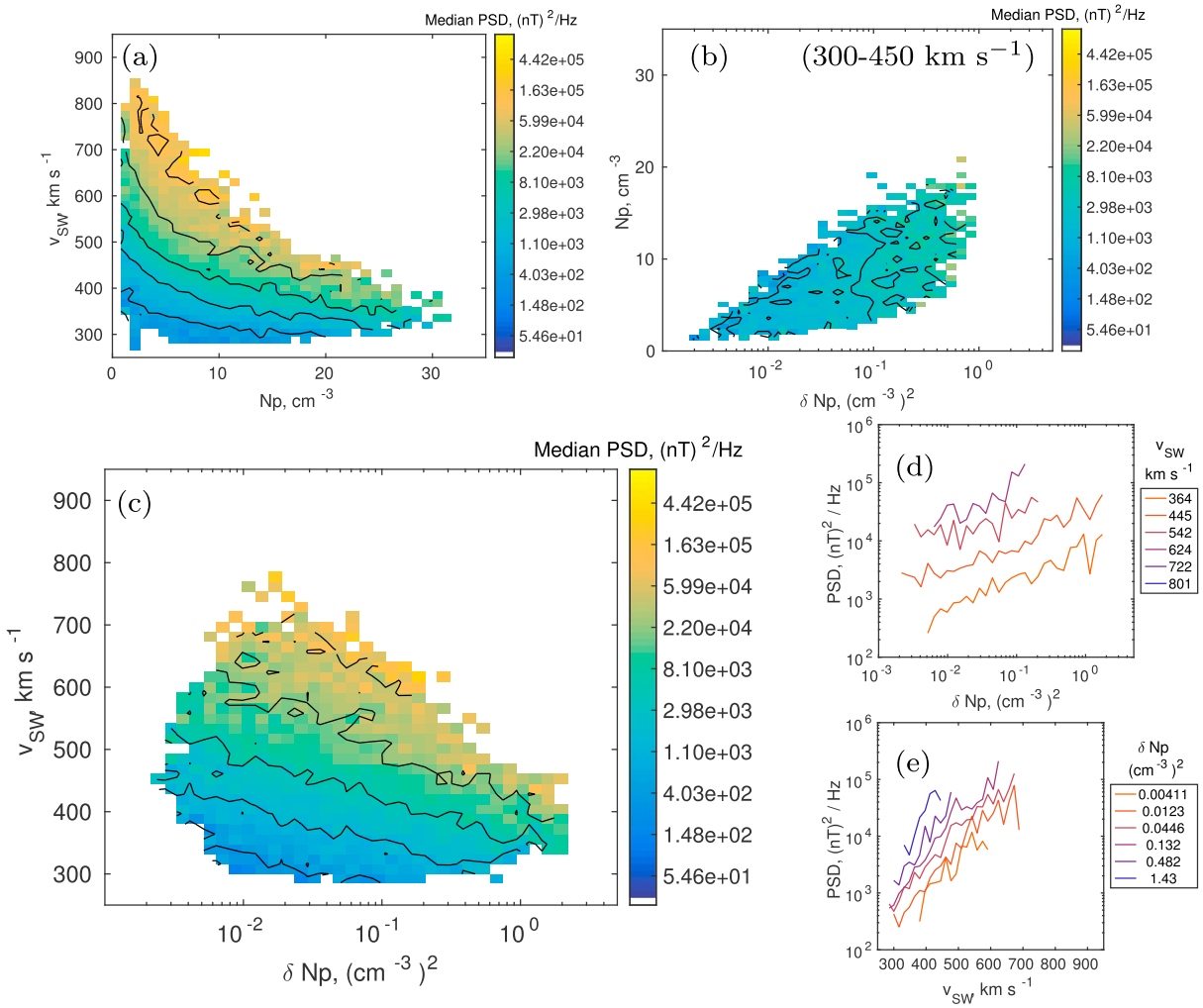

Figure 5. Data are binned by two solar wind parameters as in previous figures, and the median magnetospheric ultralow frequency power is shown. In (a) we extract the relationship of N_p and v_{sw} to magnetospheric ultralow frequency power and in (c) we do the same for δN_p. To disentangle which of N_p, δN_p is the causal parameter for this contribution, we compare the two in (b), for a single-speed bin of 300–450 km/s. Slices of constant v_{sw} and δN_p are taken from (c) and displayed in (d) and (e). PSD = power spectral density.

is 2.9×10^4 (nT)^2/Hz. For $B_z = -7.5$ nT, to get a comparable amount of power (that is, 3.0 x 10^4 (nT)^2/Hz) we only require $v_{sw} = 400$ km/s. Therefore, B_z clearly represents a significant contribution to ULF wave power and we will examine other magnetic field effects only for observations where $B_z > 0$ to remove this relationship.

As for each component B_i and their perturbations δB_i, the comparison of each component to v_{sw} and to each other is quite involved and can be found in the supporting information. We present only the component B_x here for brevity. In Figure 7 we compare the contributions from v_{sw}, B_x, and δB_x. In Figures 7a and 7b there appears to be a change in power associated with both $|B_x|$ and δB_x. Just as for N_p and δN_p, we need to establish whether this is due to the average field B_x or to the perturbations δB_x. In Figure 7c we bin by $|B_x|$ and δB_x, showing the median ULF wave power. While at first examination the power appears to be due to δB_x, this power increase follows the corresponding median solar wind speed in Figure 7d, which we know is dominant. Unfortunately, this ambiguity is not resolved by taking a single speed bin as we did for N_p in Figure 5. We find the same results for B_y, δB_y, $B_z > 0$ and δB_z (included in the supporting information as they are very similar to the results for B_x). From this initial analysis we can identify that both the mean field and the perturbations are possible contributors to ULF wave power but cannot confirm whether one or both are causal.

We must therefore examine whether any apparent contribution from components B_i or δB_i is due to a correlation between B_i and δB_i or between existing causal solar wind parameters. We have already controlled for $B_z < 0$ contributions (by only considering hours where $B_z > 0$) and for v_{sw} contributions (by choosing speed

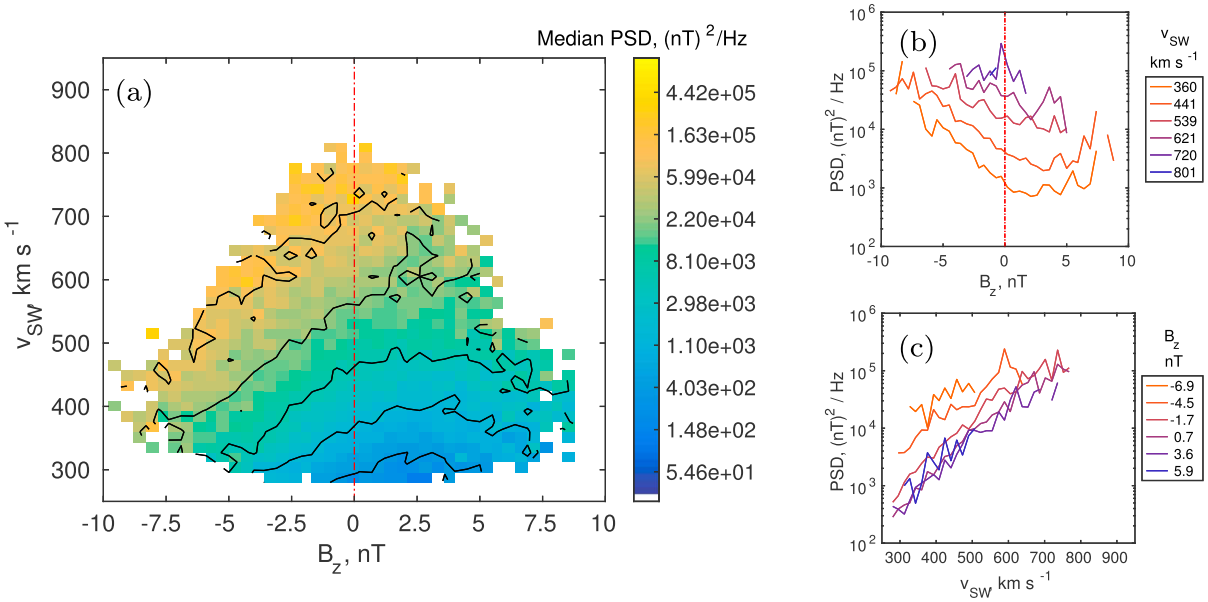

Figure 6. (a) Power spectral density (PSD) observed at 2.5 mHz at GILL is binned using the solar wind parameters speed v_{sw} and the B_z component of the interplanetary magnetic field of the preceding hour. The median PSD in each bin is shown. A red line at $B_z = 0$ is included to show the change of behavior across positive and negative B_z. Cut-throughs at constant v_{sw} and B_z are shown in (b) and (c).

to be one of our binning parameters). However, δN_p has not been controlled, which also makes an independent contribution. This is necessary as we know that δB_i and δN_p are not independent and often occur in similar types of solar wind, in particular, the sheath region before CMEs. They also inherit relationships from wave processes and from B_i and N_p, as discussed in section 3. To resolve this we take only data where $B_z > 0$ and $\delta N_p \in [10^{-2}, 5 \times 10^{-1}]$ cm^{-3} to remove these effects. Then it remains to deconvolve the pairs v_{sw} and δB_i, and v_{sw} and B_i, which we present for the x component in Figure 8. (Similar results for y and z components can be found in the supporting information). Here we can see that once δN_p has been controlled, there is no contribution to ULF wave power from B_x or δB_x when compared to v_{sw}. Hence, we conclude that components $B_{x,y}$ and perturbations $\delta B_{x,y,z}$ are not "causal" parameters and do not indicate a separate physical mechanism, instead reflecting the results for δN_p because large values of $\delta B_{x,y,z}$, $B_{x,y,z}$ and δN_p often appear in similar types of solar wind.

To summarize, we can see a clear contribution to power from B_z when $B_z < 0$ independently of the contribution from the dominant driving parameter v_{sw}. Apparent contributions from $B_{x,y}$ and/or $\delta B_{x,y,z}$ are in fact due to correlations with δN_p. It is unclear whether there is increased ULF power correlated with increasing $|B_i|$ or δB_i because the effect is small and cannot be deconvolved from v_{sw} and δN_p while retaining enough data. Therefore, of all the magnetic field parameters we only consider $B_z < 0$ as an additional causal driving parameter.

4.5. Temperature

In general, proton temperature T increases with v_{sw} although the low temperature inside CMEs may create other relationships. In Figure 9 we examine median PSD as a function of v_{sw} and T, and v_{sw} and δT. We see that ULF power increases with v_{sw} but that T appears to contribute little in comparison. Examining δT_p we see that this also does not appear to contribute to magnetospheric power.

4.6. Angles of Solar Wind Bulk Flow and IMF Orientation

These do not contribute any further information and simply confirm conclusions from earlier in this section using components v_i and B_i. They are included in the supporting information for completeness.

4.7. Dynamic Pressure P_{dyn} and Perturbations δP_{dyn}

Using our definitions above, P_{dyn} is a "derived" parameter (it is calculated using $N_p v_{sw}^2$ in the OMNI data set). Physically, it is often implicated in ULF driving (see, e.g., references above in section 1). However, while there is some correlation between v_{sw} and N_p (or δN_p) due to solar wind structure, this correlation is inherently easier to deconvolve than v_{sw} and P_{dyn}, making N_p a better choice to construct an orthogonal basis of solar

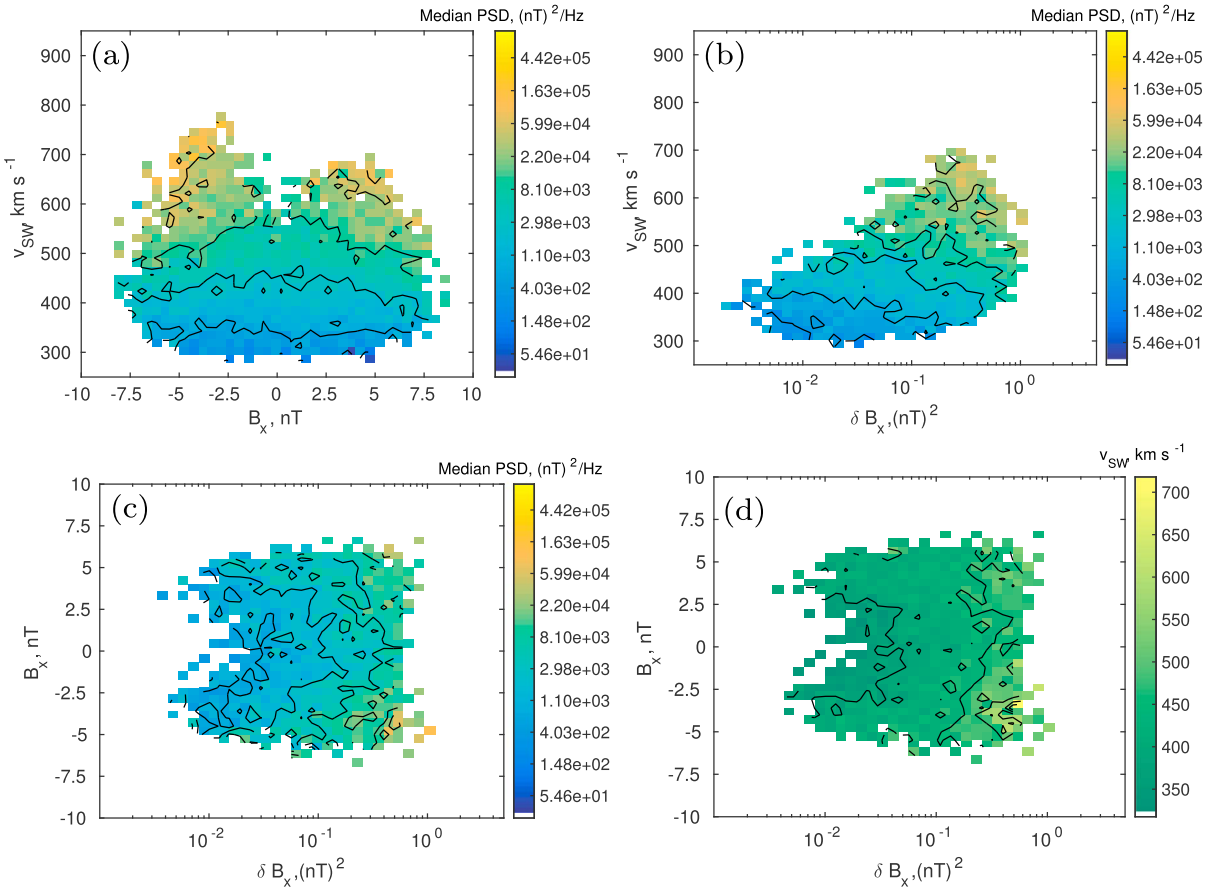

Figure 7. Observations (for $B_z > 0$ only) are binned by (a) v_{sw} and B_x, (b) v_{sw} and δB_x, (c) B_x and δB_x, and the median power spectral density at GILL, 2.5 mHz is shown. In (d) we show the corresponding median solar wind speed v_{sw} for each bin in (c). PSD = power spectral density.

wind input parameters. We therefore consider N_p in this paper instead of P_{dyn}. For completeness and comparison with previous work, two-parameter plots for P_{dyn} and δP_{dyn} are shown in the supporting information (Figures S15 and S16).

4.8. Summary of Contributing Parameters

We have analyzed all available nonderived solar wind parameters and their perturbations: v_{sw}, $v_{x,y,z}$, δv, N_p, δN_p, $B_{x,y,z}$, $\delta B_{x,y,z}$, T_p, δT_p, flow, and IMF angles. These have been analyzed in a systematic manner to account for interdependencies and identify causal properties.

We have identified the following parameters as characterizing increased ULF power in the radiation belts and hence indicators of physical mechanisms coupling solar wind activity to magnetospheric ULF wave power:

1. v_x (or v_{sw})
2. $B_z < 0$
3. δN_p

While other parameters than those above may still contribute to ULF wave power, that contribution is too small to be observed. With a larger data set we could explore other parameters in more detail but $v_{sw}, B_z < 0$ and δN_p will remain dominant. We note that the clear threshold at $B_z = 0$ indicates that in general we should consider treating $B_z < 0, B_z > 0$ separately as they represent two different regimes for ULF wave generation.

The goal of this work was to identify driving parameters in the solar wind (particularly those secondary to v_{sw}) and to discuss the mechanisms they represent, which we will do in the next section. First, we can compare δN_p and B_z to establish the order of dominance, which we show in Figure 10. We see that as expected, when controlling for v_{sw}, for $B_z > 0$ any change in power is due to δN_p, although there is some leakage near the threshold $B_z = 0$. We can also see that for $B_z < 0$, it is B_z that dominates over any δN_p contribution.

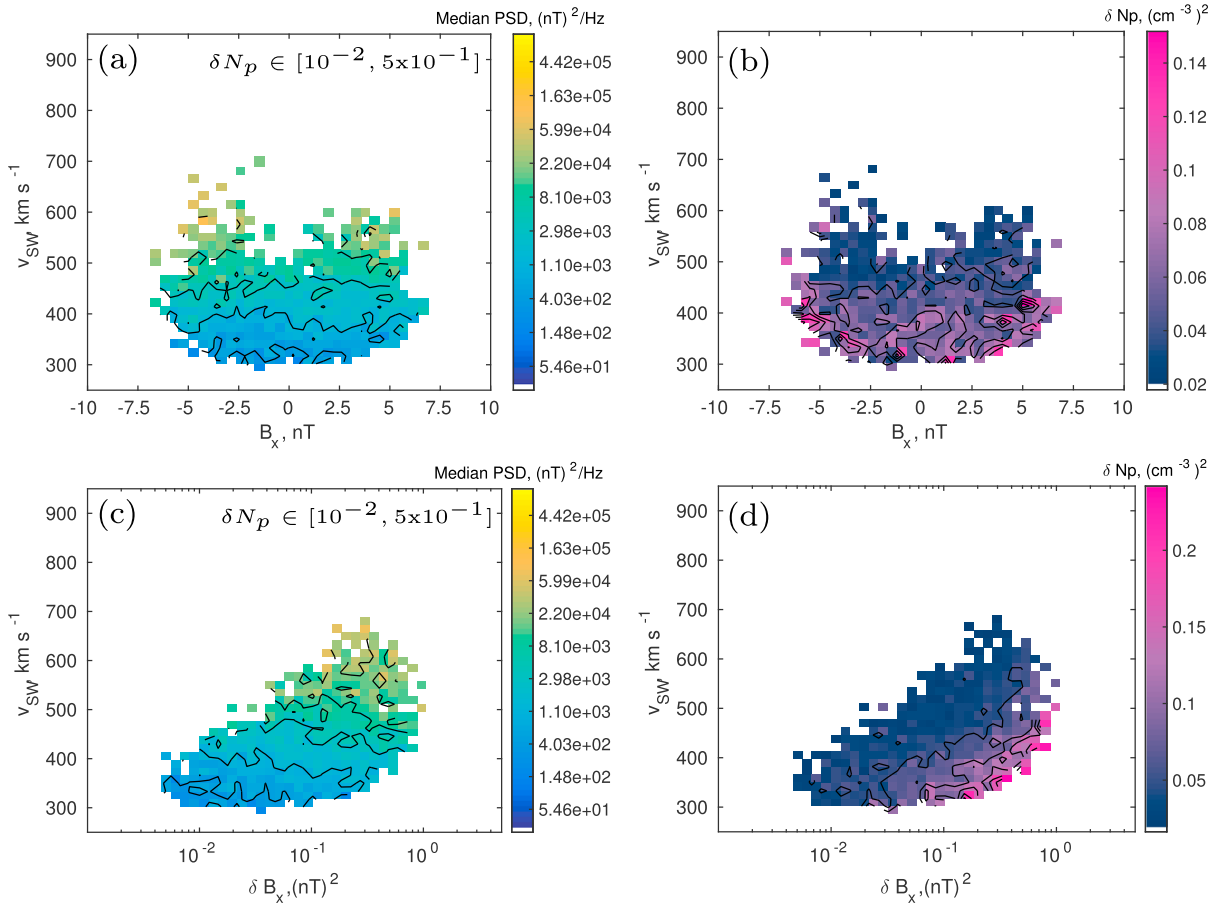

Figure 8. For $B_z > 0$ and $\delta N_p \in [10^{-2}, 5 \times 10^{-1}]$, (a) and (c) are the same as Figures 7a and 7b, where we bin by solar wind speed and B_x, δB_x, respectively, and display the median power spectral density at GILL station, 2.5 mHz. Panels (b) and (d) show the corresponding median perturbation δN_p in each bin. PSD = power spectral density.

Since the increases in power here do not follow the increases in median v_{sw} (bottom panel) and in fact the contours for median power and median speed are perpendicular to one another, we can be sure that the apparent dominance of $B_z < 0$ over δN_p is not due to any correlation with v_{sw}. Hence, the parameter contributions in order of dominance is v_{sw}, then δN_p for northward IMF, and v_{sw}, B_z, and δN_p for southward IMF.

We also briefly consider the additional effect of introducing compression regions (i.e., higher δN_p) and/or negative B_z on the median-observed PSD for the same speed bin in the table of Figure 10. Individually, both δN_p and B_z contribute noticeably to the overall power. Note that we have not chosen particularly high δN_p or strongly negative B_z due to data constraints, yet for this particular speed bin, their joint contribution results in ULF wave power an order of magnitude higher. Initial results for bins at higher speed indicate that δN_p and B_z can individually account for up to an extra order of magnitude of PSD each, and slightly more than an order of magnitude when combined. This effect will need to be quantified more thoroughly in future work in order to more accurately predict magnetospheric ULF wave power.

5. Physically Interpreting External ULF Generation Mechanisms

Having isolated the solar wind parameters which drive ULF power entering the radiation belts, we can begin to identify the physical mechanisms that they characterize. Note that we are not attempting to find any quantitative details of the dependence of ULF power on each parameter in this paper; we only identify whether each causal parameter corresponds to a monotonic increase (or decrease) in observed ULF power. An empirical formula for the dependence of ULF wave power on solar wind parameters is desirable and will be pursued in future work. We use the causal parameters v_{sw}, δN_p, and $B_z < 0$ to distinguish possible physical mechanisms and hence the plasma processes implicated in the creation of ULF waves. While we are considering

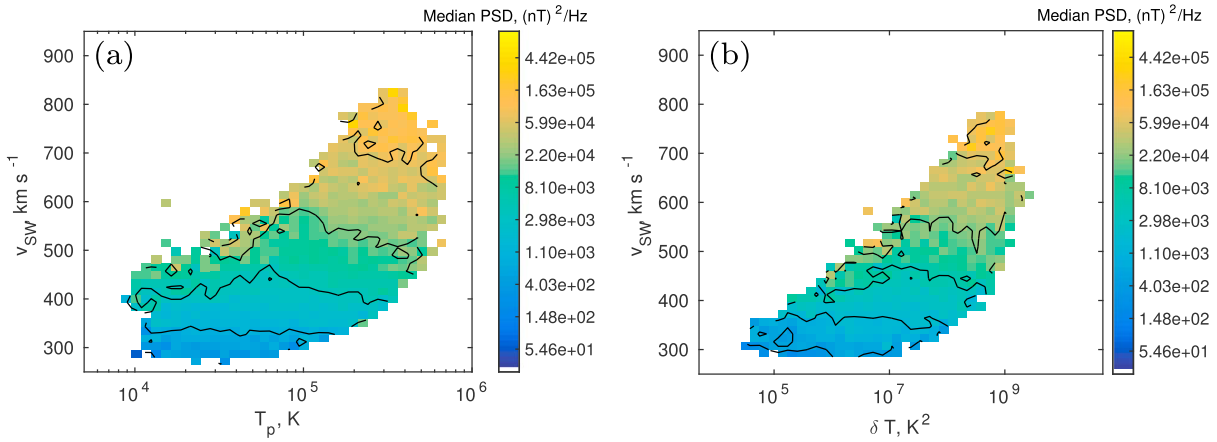

Figure 9. Data binned by (a) v_{sw} and T and (b) v_{sw} and δT. The median power spectral density (PSD) at GILL at 2.5 mHz is shown, as in Figure 4.

each mechanism separately here, in reality they are often difficult to distinguish. Indeed, they may be actively driving ULF waves concurrently and even interacting with each other.

Since solar wind dynamic pressure variations are implicated in several magnetospheric ULF wave generation mechanisms, we are obliged to begin with a discussion of the interdependence of dynamic pressure $P_{dyn} = m_p N_p v_{sw}^2$ with our causal parameters v_{sw} and δN_p, where m_p is the proton mass. In particular, we consider the magnitude of possible perturbations of P_{dyn}. A pressure perturbation δP_{dyn} could be composed of perturbations δN_p, δv_{sw}, or both. However, the comparative size of median mass density perturbation amplitude $\rho_1 = m_p N_{p_1}$ to the median background mass density $\rho_0 = m_p N_{p_0}$ is far larger than the same ratio for speed perturbations. We calculate these to be $\frac{\rho_1}{\rho_0} \sim 0.69$ and $\frac{v_1}{v_0} \sim 0.09$, respectively, from our data set. This suggests that we would not necessarily expect δv to contribute meaningfully to dynamic pressure perturbations in the solar wind.

5.1. Kelvin-Helmholtz Instability and v_{sw}

The Kelvin-Helmholtz instability (KHI) is an instability that arises from a velocity shear between two contiguous fluids. The same instability can be found in plasma. At the magnetopause Kelvin-Helmholtz waves have been demonstrated to be potential drivers of Pc3–5 ULF waves in the radiation belt region, as theoretical drivers of field line resonances (Chen & Hasegawa, 1974), by modeling throughout the magnetosphere (Walker, 1981) and by observations of ULF waves, whose energy appeared to derive from surface KHIs (Agapitov et al., 2009; Rae et al., 2005).

The incidence of Kelvin-Helmholtz waves at the magnetopause has been established by Kavosi and Raeder (2015), who showed that there appears to be no lower v_{sw} threshold to observe Kelvin-Helmholtz waves and that their occurrence increases with increasing nonshocked solar wind speed. They also confirm that Kelvin-Helmholtz waves occur at all IMF values, although they are less common for a southward IMF. As Kelvin-Helmholtz waves occur more often with increasing solar wind speed, we can assume that the causal parameter v_{sw} represents this mechanism, although the relationship may be quite complex. For example, Mann et al. (1999) and Mann and Wright (1999) demonstrate that at high enough speed ($v_{sw} \sim 500$ km/s), the boundary along the flanks of the magnetosphere becomes "overreflecting"; that is, incident fast-mode compressional waves from the magnetosphere are reflected with increased amplitude. This would increase the ULF effectiveness of Kelvin-Helmholtz waves at higher solar wind speeds.

While v_{sw} counted for the largest contribution to power in section 4, we must examine the v_{sw} dependence of other possible mechanisms before we can assert that v_{sw} represents the KHI and that Kelvin-Helmholtz boundary waves are the dominant driver external driver of magnetospheric ULF waves.

5.2. The Rayleigh-Taylor Instability

The Rayleigh-Taylor instability (RTI) occurs between two fluids of different densities where the lighter fluid is accelerated into the heavier one. Mishin (1993) demonstrated that growth rates of instabilities are increased while the magnetopause is under an accelerated motion, adding to the KHIs predicted for plasma under a velocity shear. When the magnetosphere is experiencing an expansion, the less dense magnetospheric

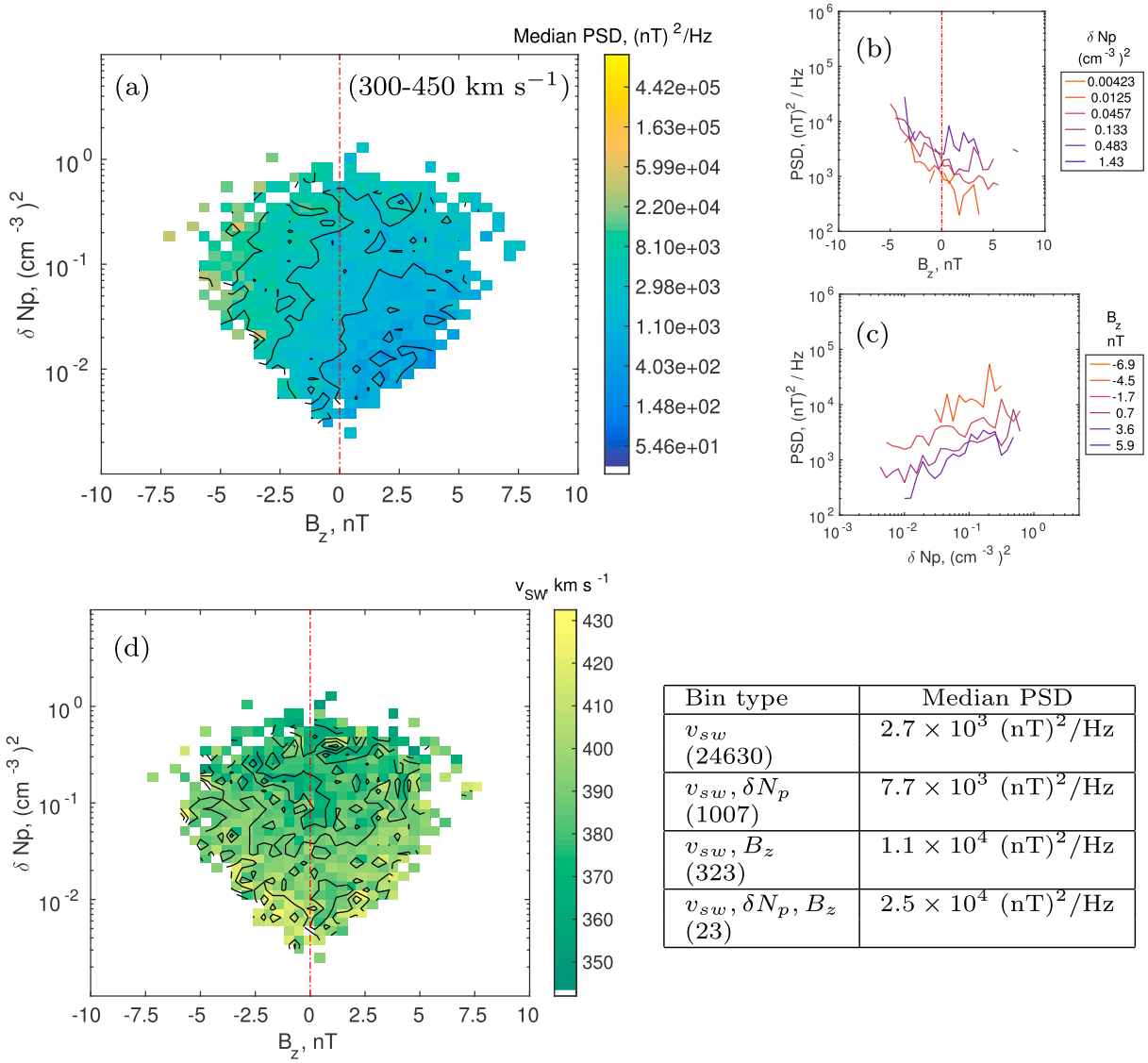

Bin type	Median PSD
v_{sw} (24630)	2.7×10^3 $(\mathrm{nT})^2/\mathrm{Hz}$
$v_{sw}, \delta N_p$ (1007)	7.7×10^3 $(\mathrm{nT})^2/\mathrm{Hz}$
v_{sw}, B_z (323)	1.1×10^4 $(\mathrm{nT})^2/\mathrm{Hz}$
$v_{sw}, \delta N_p, B_z$ (23)	2.5×10^4 $(\mathrm{nT})^2/\mathrm{Hz}$

Figure 10. We take only data between 300 and 450 km/s to control for speed. In this interval we bin by δN_p and by B_z and take the median-observed power spectral density (PSD) in the magnetosphere (a). Cut-throughs at constant B_z and δN_p are on the right, and the median speed in each bin can be found in (d) so we can check for any remaining velocity correlations. In the table (lower right) we take four selections of data and display the corresponding median PSD for all data in that bin. This is performed for combinations of the speed bin (300 to 450 km/s), a δN_p bin (5×10^{-1} to 1 $(\mathrm{cm}^{-3})^2$) and a $B_z \sim -5$ nT bin, (−5.25 to −4.75 nT). The values in brackets in the first column indicate the number of data points in that bin.

plasma pressing on the denser plasma in the magnetosheath can then become Rayleigh-Taylor unstable. Further studies by Gratton et al. (1996) and Farrugia et al. (1998) showed that the growth of these instabilities is dependent on local time, latitude, IMF conditions, and the thickness of the boundary layer. In particular we can expect a dependence on v_{sw}, N_p, and their perturbations, although as the KHI also depends on these it is unlikely we would be able to distinguish a RTI contribution using these parameters. We may expect δP_{dyn} (and hence δN_p and δv_{sw}) to represent an additional Rayleigh-Taylor contribution to the instability because they contribute to pressure perturbations and hence the resultant expansions and contractions of the magnetosphere. We would not necessarily see this for δv_{sw}, as discussed in the beginning of this section.

While the difficulty in distinguishing the contribution of individual mechanisms to ULF wave power is discussed in section 5.6 we note here that the RTI is particularly challenging to isolate. First, pressure perturbations themselves constitute a distinct driving mechanism (see section 5.3). Second, the RTI requires an acceleration of the magnetopause and the resulting effect will simply add to KHI growth rates, making it difficult to distinguish the contribution of RTI to magnetospheric ULF wave power. Future theoretical work

is required in this area to determine the additional ULF wave power from a joint RTI-KHI and to determine how well δN_p represents the Rayleigh-Taylor contribution.

5.3. Density Perturbations and Solar Wind Compressional Waves

Observations of magnetospheric ULF waves corresponding to solar wind density oscillations (Kepko & Spence, 2003) indicate that the movement of the magnetopause in response to solar wind dynamic pressure P_{dyn} changes can enable generation of fast-mode compressional waves; a sudden decrease in solar wind dynamic pressure allows the magnetosphere to expand, resulting in a decrease in the magnetospheric magnetic field. Conversely, a sudden increase in P_{dyn} compresses the magnetosphere resulting in an increase in the magnetic field. These magnetic field perturbations then propagate inward. This mechanism does not need to be global; variations in the shocked magnetosheath could constitute local generation of fast-mode compressional waves.

However, the source of these ULF-effective pressure perturbations in the solar wind is unclear. The proposed origins can be considered in two ways: (1) solar wind "structures" that change slowly, are fixed with respect to the plasma and are swept past the Earth, and (2) plasma processes which (mainly through processing in the foreshock) can interact with the Earth's magnetosphere as they evolve rather than being swept past. Examples of the first are entropy waves and sheath regions, and examples of the second include propagating magnetohydrodynamic (MHD) waves and magnetosheath instabilities. Of course, using OMNI data we can only examine the response to MHD waves observed near L1. In particular, Walker (2002) studied the possibility of coherent solar wind MHD waves carrying density perturbations and driving magnetospheric ULF waves via transmission through the bow shock and subsequent incidence upon the magnetopause. We are able to use the analysis developed in section 4 to compare these two views of solar wind driving by pressure perturbations.

Specifically, we can investigate whether solar wind compressional waves are ULF-effective by looking at the causal parameters found previously. If the power increase is only due to structures sweeping past, both δN_p and δv_{sw} would affect magnetospheric power as they indicate pressure perturbations and hence perturbations of the location of the magnetopause—although at the beginning of section 5 we have already discussed that δN_p will give rise to larger pressure perturbations δP_{dyn}, so we may not resolve any such direct δv_{sw} contribution. If the cause of the pressure perturbations is instead predominantly from compressional waves in the solar wind, we would expect relationships between δN_p, δv_{sw}, and $\delta B_{x,y,z}$ following plasma wave theory. That is, for a given mass density perturbation amplitude ρ_1 at a single frequency, we can estimate the magnitude of corresponding speed perturbation amplitude $|\mathbf{v}_1|$ for a compressional wave in the solar wind. If these perturbations are within our resolution, we would expect to also see a relationship between increased magnetospheric ULF wave power and $|\mathbf{v}_1|$ (and hence δv_{sw}) when compressional waves are active.

As described in the appendix, we use the median amplitude of number density perturbations $N_{p_0} \sim 3.7$ cm^{-3} at 2.5 mHz to find a range 44–106 km/s for the corresponding speed perturbation amplitude of an "average" wave. Velocity perturbations of this size are clearly within our resolution. Therefore, we can rule out coherent compressional waves as ULF drivers as follows: To identify whether compressional waves are the mechanism, we first assume that the majority of ULF-effective δN_p are due to compressional waves. If this assumption is true, then every time we see increased δN_p we would expect to see increased δv within our visible range and hence a corresponding correlation between δv and ULF power. However, we do not see this δv correlation. Therefore, there can be no particular relationship between δv and δN_p at the times when δN_p is ULF-effective, which is only possible if the predominant origin of ULF-effective δN_p (and hence δP_{dyn}) is not compressional waves. This suggests that the ULF-effective δN_p are instead due to structures sweeping past the magnetosphere.

5.4. Perturbations Arising at the Bow Shock or in the Magnetosheath

While we have considered ULF waves observable in the solar wind near L1, perturbations can also arise between L1 and the magnetosphere. Near the bow shock, transient ion foreshock phenomena (such as hot flow anomalies, among other phenomena) have been shown to drive magnetospheric ULF waves in our range of interest (e.g., Archer et al., 2013; Hartinger et al., 2013; Wang et al., 2017) both directly and via waves modes arising from the resulting magnetosheath instabilities; these foreshock origin ULF waves are then convected downstream to "ring" against the magnetopause (e.g., Hwang & Sibeck, 2016). Although these mechanisms are all external drivers, they occur downstream of L1 and it is unclear how our solar wind parameters relate to these, particularly in an hour-long window when these are relatively rare events and so may not show up

in our analysis. For example, Schwartz et al. (2000) found that hot flow anomalies occur ~3 times a day and only last a few minutes. We note that Hartinger et al. (2013) found that ULF waves around our frequency range driven by ion foreshock phenomena correlate with dynamic pressure pulses in the ion foreshock. Indeed, the dependence of ULF waves on δN_p may be indicative of this effect but we cannot distinguish the effect of density perturbations observed at L1 and the amplification of this in the magnetosheath. Therefore, we consider these mechanisms to be "post-L1 processing" and cannot extract their role explicitly in the generation of magnetospheric ULF waves.

5.5. Flux Transfer Events, Reconnection and $B_z < 0$

In section 4.4 we identified that B_z was a causal parameter during southward IMF, that is, when below the threshold $B_z = 0$. Since we know that strongly negative values of B_z correlate with higher reconnection rates at the dayside magnetopause (Komar & Cassak, 2016), we look at how this could relate to the generation of magnetospheric ULF waves.

Bursty reconnection has been associated with the formation of magnetic flux tubes called "flux transfer events" (FTEs) which contain the reconnected field lines and constitute a plasma entry mechanism to the magnetosphere. They have long been considered a potential source of magnetospheric ULF waves (Russell & Elphic, 1978), and simultaneous observations of FTEs and 2–7 mHz waves in the magnetosphere were first made by Glassmeier et al. (1984). The details of this mechanism were described in more detail by Gillis et al. (1987), who also estimated that the resultant waves would be in the 2–22 mHz range. The draping of the magnetospheric magnetic field around a flux tube results in a local increase in the magnetic field outside the event (Farrugia et al., 1987; Paschmann et al., 1982) as confirmed by observations of FTEs perturbing the magnetosphere as they propagate (Liu et al., 2008). If we consider the plasma to be compressible, then we would also expect to see accompanied local increases or decreases in the density outside the flux tube as it propagates along the magnetopause. This movement has a rippling effect on the magnetospheric boundary and as the flux tube is pulled along tailward, driving fast-mode waves in the magnetospheric plasma which propagate inward and can couple with the field line to drive standing waves.

While we are studying external drivers in this paper, we also note that the IMF B_z may additionally characterize ULF waves driven by substorms such as those generated directly by bursty bulk flows, by velocity shears in these flows, or from instabilities arising from the new particle distributions (e.g., McPherron, 2005, and references within). However, they would be associated with a time lag rather than our instantaneous interval (Cowley & Lockwood, 1992) and are also from a short-lived source compared to external driving sources. As we are averaging over hour timescales and using dayside data, we therefore consider the ULF power increase with B_z to predominantly represent flux transfer events rather than substorm activity.

5.6. Distinguishing Potential Driving Mechanisms From the Dominant Solar Wind Parameters

It remains to establish which mechanisms the parameters v_{sw}, $B_z < 0$, and δN_p represent as we have only considered them individually, not as a whole, and we have not discussed their interdependence.

The dependence of ULF wave power on δN_p could provide evidence for either a RTI or a pressure (i.e., density) perturbation contribution. For the RTI we would expect to see additional growth rates of boundary instabilities which are already dominated by v_{sw}. Instead, we believe δN_p represents the pressure perturbation theory as there is clear evidence of this acting as an individual mechanism; there have been observations of the same discrete frequencies in both solar wind pressure oscillations and magnetospheric ULF waves (Kepko & Spence, 2003). If there is an extra contribution from the Rayleigh-Taylor mechanism, it is subordinate to the others discussed in this paper; it is also possible that RTI contributions do not show up due to our hour timescale. Future work could investigate the necessary timescale.

It has been theorized that the number density affects the KHI condition (Engebretson et al., 1998), but we saw no increased ULF wave power for N_p once we accounted for δN_p. We believe that similar to the Rayleigh-Taylor effect, the additional instability growth does not contribute as much to ULF wave power as other mechanisms and so cannot be resolved.

In section 5.4 we discussed the difficulty in characterizing ULF drivers that arise downstream of L1, for example, near the bow shock and from waves generated by magnetosheath instabilities. This processing has been shown to affect ULF waves but as events such as hot flow anomalies are relatively rare, occurring ~3 times a day and lasting a few minutes (Schwartz et al., 2000), they are unlikely to show up in our statistical analysis

over 15 years. We consider it possible that such processing is a factor in the δN_p contribution observed here, but exploring the role of bow shock and magnetosheath processes in this context is beyond the scope of this study.

It has previously been noted that FTEs propagating along the magnetopause share several properties with Kelvin-Helmholtz waves (Kavosi & Raeder, 2015) and appear very much like the ripples resulting from solar wind pressure oscillations (Sibeck, 1990). These have already been established as distinct phenomena (e.g., Lockwood, 1991; Otto et al., 1995; Song et al., 1994) and now, with our study of the causal parameters, it appears that they individually contribute to ULF wave power near ~6.6 R_E. However, it is difficult to compare the relative contributions of each mechanism using just the three parameters v_{sw}, $B_z < 0$, and δN_p as they share solar wind parameter dependencies. In addition to this, these mechanisms can interfere with each other. For example, while the strongest controlling factor for FTE formation is B_z (Kuo et al., 1995; Russell et al., 1996) and while the separation time of FTEs appears to be independent of our causal parameters (Wang et al., 2006), the magnetic amplitude of FTEs is weakly dependent on solar wind dynamic pressure and the rate of propagation of FTEs will depend on both the magnetic curvature force on reconnected field lines and the solar wind speed. Furthermore, it has been indicated that flux transfer events and Kelvin-Helmholtz boundary waves can interact; FTEs can provide the seed for Kelvin-Helmholtz waves and propagating FTEs can interfere with the growth of Kelvin-Helmholtz boundary waves (Hwang & Sibeck, 2016, and references therein). In fact, Kavosi and Raeder (2015) found fewer and shorter Kelvin-Helmholtz boundary waves for southward IMF. For this reason, while it is clear that for $B_z > 0$ it is Kelvin-Helmholtz waves that represent the dominant contributing mechanism, the prevalence of v_{sw} for $B_z < 0$ could indicate the dominance of either (or both) Kelvin-Helmholtz boundary waves and FTE formation and propagation as magnetospheric ULF drivers.

Note that while the magnetopause flanks are expected to be more Kelvin-Helmholtz unstable, we observed no additional contribution to power from increased nonradial flow compared to the parameters v_{sw}, $B_z < 0$, and δN_P.

We have not discussed physical properties of the magnetosphere that may affect ULF power observed at a fixed point on the ground. Particularly of relevance to this study is magnetopause location. A compressed magnetosphere will affect ground-observed power as the spatial location in the equatorial plane corresponding to any magnetometer station moves closer to the Earth, and as the distance from this point to the magnetopause decreases. For example, waves generated by a KHI at the magnetopause decay with distance from the source (Southwood, 1974), hence a closer source could cause increased ULF PSD measurements on the ground. Takahashi and Ukhorskiy (2007) discuss this as a possible cause of P_{dyn} control of ULF wave power. (Murphy et al., 2015) showed that during storm times there is a clear dependence of ground-based ULF wave power on magnetopause location and also suggested that ULF wave power may become more concentrated when the volume of the magnetosphere reduces. Since the model they used (Shue et al., 1998) depends on B_z and P_{dyn} it is clearly difficult to distinguish between the mechanisms discussed here and a simple change in the magnetopause location. We note that these dependent parameters are slightly different; N_p would be expected to correlate with P_{dyn} control of magnetopause location, yet we see increased ULF wave power with perturbations δN_p rather than with N_p. Since there is evidence for ULF driving by both flux tube propagation and solar wind density perturbations as discussed above, it is likely that the action of these drivers as observed at GILL is modulated by magnetopause location. As magnetopause location is dependent on B_z and P_{dyn} (as calculated in Shue et al., 1998, and used in Murphy et al., 2015) this makes it very difficult to determine just how much each physical process contributes to ULF wave power.

One result of interest is the clear dominance of $B_z < 0$ over δN_p, even though they represent physically very similar mechanisms; a direct deformation of the magnetopause causing perturbations of density and the magnetic field. Because we cannot know how well the parameters B_z and δN_p represent their respective mechanisms, and how much these parameters also represent modulation by magnetopause location, we cannot be certain that FTEs are truly more ULF-effective than solar wind density perturbations. It is possible that not all perturbations δN_p are ULF-effective and so their apparent parameter contribution is diminished, or it may be that broadband power δN_p is not the most relevant method of considering density perturbations. We suggest that further work is necessary to more precisely quantify the contributions of all of these mechanisms, which are highly interdependent.

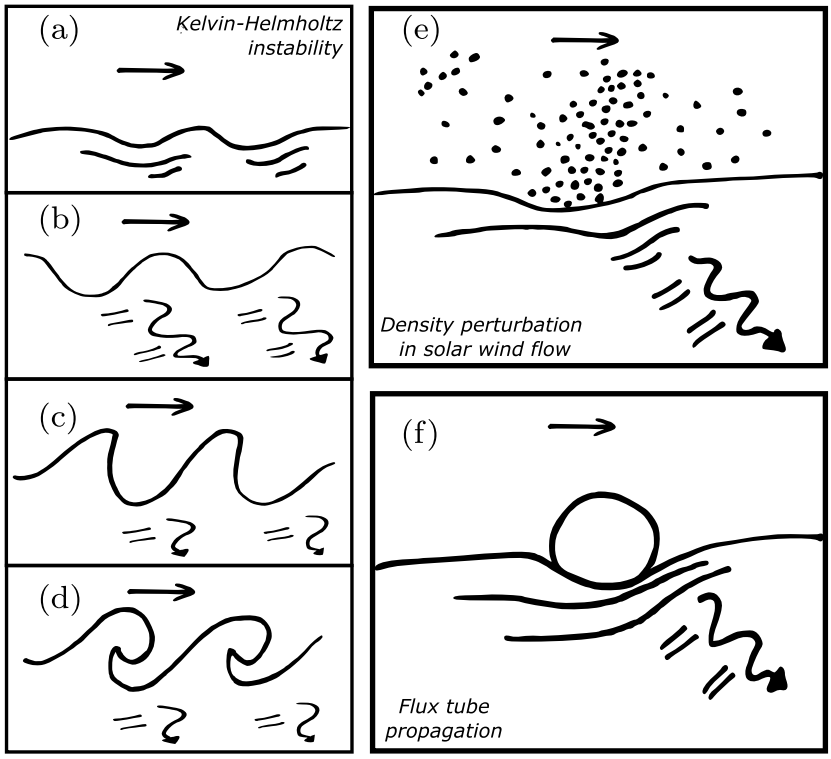

Figure 11. The three main driving mechanisms by which the solar wind directly gives rise to magnetospheric ultralow frequency waves, depicted idealistically. In (a)–(d) the Kelvin-Helmholtz instability grows from an initial perturbation. The velocity shear between the magnetosphere and the faster solar wind means that this mode is unstable; troughs deepen while peaks grow. Compressional waves are launched in the magentosphere which propagate inward, while eventually, the instability develops into vortices. Panel (e) depicts the direct driving of compressional waves by a proton number density perturbation, where there is a velocity component normal to the magnetopause. A region of more dense plasma perturbs the magnetospheric boundary, and the resulting compression of the magnetospheric magnetic field is propagated inward. Similarly in (f), a flux tube is shown as a rigid cylinder propagating along the magnetopause. The draping of the magnetic field around this tube as it travels launches earthbound compressional plasma waves. In reality these mechanisms may well co-occur and interact, and their effectiveness will be moderated by magnetosphere configuration such as the location of the magnetopause.

5.7. Summary of Contributing Mechanisms

We conclude that the three dominant external generation mechanisms for magnetospheric ULF waves are the (1) KHI, (2) the formation and/or propagation of flux tubes, and (3) direct driving by solar wind density perturbations, which result from solar wind structures rather than coherent compressional plasma waves in the solar wind, and may also include processing downstream of L1. These mechanisms are depicted in Figure 11; note that all these theories involve magnetopause deformations of some kind. For $B_z > 0$ it is clear that Kelvin-Helmholtz waves are the dominant ULF drivers, while it is unclear whether this holds for $B_z < 0$ as FTEs share many driving parameters with (and interact with) Kelvin-Helmholtz waves.

6. Discussion

Previous studies using ground-based magnetometers have concentrated on the dependence of ULF wave power as a function of L-shell and MLT (e.g., Mathie & Mann, 2001; Pahud et al., 2009). In this paper, we have adopted a different approach in order to identify the dominant driving mechanisms. We have accounted for solar wind parameter interdependencies; controlling for v_{sw} clearly reveals the ULF wave power dependence on δN_p and B_z. Wolfe (1980) is an early example of a similar approach, using stepwise multiple regressions to identify that v_{sw} is the dominant parameter and that N_p is a likely second. However, they could not deconvolve the nonlinear relationship between v_{sw} and N_p with their limited amount of data, in contrast to the large data set available here. A regression approach also assumes a continuous relationship between two parameters, whereas here we found a distinct threshold at $B_z = 0$. More recently, Baker et al. (2003) compared field

line resonance (FLR) and non-FLR characteristics and found that v_{sw}, N_p, and B_z affected near-monochromatic ULF wave activity in the form of FLRs. However, they discounted N_p as to first order, any N_p contribution was due to an anticorrelation with v_{sw}. Baker et al. (2003) also found that $B_z > 0$ had a slightly stronger effect than $B_z < 0$, unlike in our analysis. The reason for this discrepancy is unclear, although it is possibly due to the fact that they focused on field line resonances and near-monochromatic activity where we have considered all ULF activity at 2.5 mHz. Indeed, the differences noted in Baker et al. (2003) for FLR versus non-FLR ULF wave activity indicate that future work is needed on their respective generation mechanisms and subsequent propagation. Simms et al. (2010) used path analysis to control the interdependencies between nonderived solar wind parameters affecting a ULF wave index and found $v_{sw} and B_z$ to be the main parameters with an additional contribution from *Dst* and variations in number density and IMF. In contrast, we too found v_{sw}, $B_z < 0$, and δN_p to dominate ULF power but could not resolve any additional δB contribution. We also found that the B_z contribution has an onset threshold at $B_z = 0$. Our comprehensive and systematic analysis of all nonderived parameters has shown that nonlinear solar wind interdependencies do indeed impact the resultant parameters correlating with power. In general our results match those of the ground-based studies, with v_{sw} the dominant driver around geosynchronous orbit. While Takahashi et al. (2012) found that the dominant driver switched to variations of P_{dyn} at lower L-shells, we do not extend to these L-shells in this study.

Baker et al. (2003), Pahud et al. (2009), and Takahashi et al. (2012) found that ULF wave dependence on solar wind parameters varied with MLT. Throughout this work we have focused on 3–21 MLT, but have confirmed these results for individual MLT sectors (Figures S18–S21 in the supporting information). To summarize, we find some minor differences between nonmidnight sectors (dawn, noon, and dusk) but the same parameter dominances v_{sw}, $B_z < 0$, and δN_p. We find the same parameters v_{sw}, B_z, and δN_p for the midnight sector, but the threshold $B_z = 0$ does not hold. We intend to confirm these results quantitatively in future work.

In this study we chose to examine only instantaneous power. Using time lags would allow us to account for substorm contributions, which we expect to correlate roughly with time-lagged B_z (Cowley & Lockwood, 1992), as substorm onset can be described using as a probability distribution (Freeman & Morley, 2004). However, it would be difficult to properly account for time-lagged interdependencies, particularly as solar wind properties change with the solar cycle. For example, solar wind speed persists for several hours while B_z does not (Lockwood et al., 2016; Owens et al., 2017). Similarly, to include the initial state of the magnetosphere, we would need to know more about the persistence of existing ULF waves. Therefore, using instantaneous magnetospheric ULF wave power eliminates these questions by "averaging" over any previous history. Furthermore, we expect an hour timescale to be sufficient time for the generation of ULF waves by the external sources discussed in section 5. Future work could involve the development of a more sophisticated approach to determine optimal time lags while controlling solar wind parameter interdependencies. Additionally, the interactions between these proposed drivers and the role of magnetosheath processes could be explored.

We have produced manageable results by using only a single frequency at a single station (and therefore at a narrow range of L-shells) over dayside magnetic local times. A brief look at the results for other stations, other frequencies, and the geomagnetic east-west coordinate provides the same qualitative results (i.e., the same causal parameters in the same order of dominance). The development of a quantitative approach to compare these meaningfully will be greatly simplified by the use of the three parameters established here. It is clear that the inclusion of these subordinate parameters is important; for example, the observed ULF wave power spectral density for $v_{sw} = 600$ km/s and $B_z > 0$ nT is comparable to a speed of only 400 km/s if $B_z = -7.5$ nT.

7. Summary

We have performed a systematic and comprehensive series of straightforward two-parameter comparisons to identify the dominant solar wind parameters (measured near L1) contributing to magnetospheric ULF wave power. Since speed v_{sw} dominates, we begin by examining power spectral density as a function of v_{sw} and each parameter X to determine whether each X is a potential contributing parameter, then examine all remaining parameter relationships iteratively, as explained in Figure 1. This method accounts for interdependencies between parameters, revealing subordinate contributions which we have used to consider physical processes by which ULF waves can be generated. Our main results are as follows:

1. ULF wave power increases for increasing v_{sw}, strongly negative $B_z < 0$, and increasing perturbations δN_p. All three parameters contribute significantly to the total power.

2. Considering interdependencies is important: in particular, we find that δN_p contributes to ULF wave power rather than N_p. Interdependence is difficult to sort out as the relationships between parameters are not simply linear. Furthermore, the ULF driving mechanisms themselves are also highly interdependent.
3. We find we must consider hours with $B_z < 0, B_z > 0$ separately and this may be necessary elsewhere. There are no such onset thresholds for v_{sw} and δN_p contributions to ULF wave power.
4. We conclude that the three dominant external generation mechanisms are the KHI, flux tube events during bursty reconnection, and solar wind density perturbations deforming the magnetopause. For northward IMF ($B_z > 0$) the KHI is the dominant mechanism. For southward IMF it is unclear whether the KHI or FTEs are dominant, although both are more ULF-effective than solar wind density perturbations. It is unknown how magnetopause location modulates the effectiveness of these processes.
5. ULF-effective solar wind density perturbations can be attributed to solar wind structures (spatial variations in the solar wind sweeping past) rather than compressional waves originating in the solar wind. We have not considered the processing of these variations between L1 and the magnetopause.

Our straightforward but systematic approach has focused on controlling the assumptions and examining which driving parameters can be ruled out. This reduction to three main parameters and three main external driving mechanisms can be used to discover more about the physical processes involving magnetospheric ULF waves and to predict power in the radiation belts.

We have observed that simple parameterizations dependent only on v_{sw} cannot fully describe the magnetospheric ULF wave power because δN_p and B_z both represent significant contributions. Therefore, to be able to characterize ULF wave power fully, we will need to consider the effects of multiple physical mechanisms acting simultaneously; a flip to B_z southward or a sudden compression region striking the magnetosphere will result in higher ULF power observed in the radiation belt region. While v_{sw} predominantly determines the magnetospheric ULF wave power, the additional contribution of masked subordinate mechanisms is significant and needs to be considered if we are to be able to predict ULF wave power and hence properties of the electron population near geostationary orbit.

Appendix A: Fast-Mode Compressional Waves Corresponding to Observed Density Perturbations δN_p

In section 5.3 we used the properties of fast-mode compressional waves to identify the source of solar wind pressure perturbations. Here we confirm that the relationship between the amplitude of number density and velocity perturbations would be detectable using our solar wind observations. We derive this relationship and justify the extent to which it is valid.

Here we consider the possibility that ULF-effective δN_p are a result of MHD waves originating at the Sun. While Alfvén waves may reach the Earth, they are not associated with density perturbations so we do not consider them here. Both slow- and fast-mode compressional waves are damped in high β plasmas and therefore may not reach the Earth, but slow-mode waves are far more strongly damped (Barnes, 1966). Therefore, we only use fast-mode waves in this analysis. We cannot and do not study entropy waves (i.e., density structures bound to the moving plasma) with this method.

In section 2.1 we summed the power in N_p across frequencies 1.7–6.7 mHz to find δN_p. Here we can use the power at 2.5 mHz, $\mathcal{P}_{N_p}$(2.5 mHz). The square root of this is then the amplitude of number density perturbations in that hour at 2.5 mHz, N_{p_1}. Using the median mass density perturbation amplitude at 2.5 mHz, $\rho_1 = m_p N_{p_1}$, and "average" (median) solar wind plasma values for unperturbed mass density $\rho_0 = m_p N_{p_0}$, unperturbed magnetic field $\mathbf{B}_0$, Alfvén velocity v_A and sound speed v_S, we can estimate the magnitudes for the corresponding velocity perturbations $\mathbf{v}_1$ of an "average" compressional wave. If these perturbations are of the same order as mean hourly values, then they are detectable from the background, and so we should be able to identify whether they are correlated with power at all. If the perturbations are small compared to the background we will not be able to identify whether or not they have a contribution.

We use two different coordinate systems: the GSE frame in which we have our OMNI data observations and the wave-centered frame with basis $\hat{\mathbf{a}}, \hat{\mathbf{b}}, \hat{\mathbf{c}}$. In this basis we define the $\hat{\mathbf{c}}$-direction to be along the magnetic field, the $\hat{\mathbf{a}}$-direction to be the direction of propagation perpendicular to $\mathbf{B}_0$ and $\hat{\mathbf{b}}$ to complete the set.

Table A1
Table of Median Values Used to Calculate the Resultant Size of Velocity Perturbations We Expect From Fast-Mode Compressional Waves

Parameter	Median Value
ρ_0	5.2 cm^{-3}
ρ_1	3.7 cm^{-3}
v_A	52.0 km/s
v_s	55.8 km/s
$v_{\mathrm{ph}_{\mathrm{min}}}$	55.8 km/s
$v_{\mathrm{ph}_{\mathrm{max}}}$	76.3 km/s

The parameter **k** is the direction of propagation of the wave.

$$\begin{aligned}\hat{\mathbf{a}} &= \frac{\mathbf{a}}{|\mathbf{a}|}, \quad \mathbf{a} = \mathbf{k} - (\mathbf{k}\cdot\hat{\mathbf{c}})\hat{\mathbf{c}}\\ \hat{\mathbf{b}} &= \hat{\mathbf{c}}\times\hat{\mathbf{a}}\\ \hat{\mathbf{c}} &= \frac{\mathbf{B}_0}{|\mathbf{B}_0|}\end{aligned} \tag{A1}$$

Then in this basis **k** can be written as

$$\mathbf{k} = k[\sin\theta \quad 0 \quad \cos\theta] \tag{A2}$$

where θ is the angle of propagation from the magnetic field and can also be found in the dispersion relation (Walker, 2004)

$$\left(\frac{\omega}{k}\right)^2 = v_{\mathrm{ph}}^2 = \frac{1}{2}\left[v_A^2 + v_S^2 \pm \left[(v_A^2+v_S^2)^2 - 4v_A^2v_S^2\cos^2\theta\right]^{\frac{1}{2}}\right] \tag{A3}$$

where the plus (+)symbol describes the fast mode and the minus (−) symbol the slow mode. We only use the fast mode as discussed above, which gives us an upper bound on the amplitude of velocity perturbations.

We can work out relationships with the total magnitude of perturbations ρ_1 and $|\mathbf{v}_1|$ in the wave-centered frame, which can then be applied to any orthonormal coordinate system, removing the necessity of calculating the direction of propagation. We consider the effect of the bulk streaming of the solar wind plasma later.

Using the following linearized MHD equation

$$\rho_1 = \frac{\rho_0}{\omega}\mathbf{k}\cdot\mathbf{v}_1 \tag{A4}$$

we see that there can be velocity perturbations in directions $\hat{\mathbf{a}}$ and/or $\hat{\mathbf{c}}$,

$$\frac{\rho_1}{\rho_0}v_{\mathrm{ph}} = \hat{\mathbf{k}}\cdot\mathbf{v}_1 = \hat{k}_a v_{1a} + \hat{k}_c v_{1c}. \tag{A5}$$

We can use this to put a limit on the magnitude of velocity perturbations by writing it as

$$\mathbf{v}_1 = \begin{bmatrix}v_{1a} & 0 & v_{1c}\end{bmatrix} = v_1\begin{bmatrix}\sin\theta_v & 0 & \cos\theta_v\end{bmatrix} \tag{A6}$$

describing all possible solutions in this basis using a new parameter θ_v. Then

$$\left|\frac{\rho_1}{\rho_0}v_{\mathrm{ph}}\right| = \sqrt{|\mathbf{v}_1|^2 + 2_1v^2\sin\theta\cos\theta\sin\theta_v\cos\theta_v} = |\mathbf{v}_1|\sqrt{1+2\sin\theta\cos\theta\sin\theta_v\cos\theta_v} \tag{A7}$$

and so we know the amplitude of velocity perturbations is within the range

$$\frac{1}{\sqrt{3}}\left|\frac{\rho_1}{\rho_0}v_{\mathrm{ph}}\right| \le |\mathbf{v}_1| \le \left|\frac{\rho_1}{\rho_0}v_{\mathrm{ph}}\right| \tag{A8}$$

which is independent of basis. This range will change with angle of propagation θ as v_{ph} is dependent on θ. The total range in which velocity perturbations lie for all θ and the plasma values used are shown in Table A1. We find that the maximum and minimum total speed perturbations using equation (A8) are v_{min} ~44.8 km/s and v_{max} ~106.2 km/s. This shows that for an "average" wave the speed perturbations are of an order that is distinguishable from background solar wind values.

We have not yet included the effect of the bulk flow of the solar wind plasma. The velocity along the Sun-Earth line means that for a velocity oscillation along x, corresponding velocity perturbations in the y and z components will appear to be of different frequencies. However, Walker (2002) uses the approximation that a fast-mode wave will be propagating close to the Sun-Earth line by the time it reaches us. In this case, as velocity perturbations are along the magnetic field and axis of propagation, the component of compressional wave velocity perturbations away from the bulk flow (the shifted y and z components) should be relatively small. We do not need to identify every instance of a compressional wave to study their relationship to magnetospheric ULF wave power. We do not expect any velocity perturbations to represent a negative contribution to ULF power and so even a relatively small proportion with a positive contribution would manifest by indicating that δv has some relationship with the resultant ULF power in Figure 4, which we do not see.

To summarize, the amplitude range of velocity perturbations corresponding to ULF-effective δN_p are resolved by our data. Therefore, as long as there are enough waves with these characteristics, if compressional waves are the solar wind source of ULF-effective δN_p, we would expect to see apparent increases of ULF power with the correlated δv. As we do not, the δN_p that are ULF-effective cannot come from coherent solar wind compressional waves, as concluded in section 5.

Acknowledgments
We acknowledge use of NASA/GSFC's Space Physics Data Facility's OMNIWeb service and OMNI data. The CANOPUS magnetometer array (now CARISMA, www.carisma.ca) is operated by the University of Alberta and funded by the Canadian Space Agency.
The authors thank the CARISMA team for data; in particular, Andy Kale for his help with quality control. S. N. Bentley is supported by a NERC PhD studentship through the SCENARIO Doctoral Training Partnership grant NE/L002566/1. C. E. J. W. is supported by STFC grant ST/M000885/1 and M. J. O. is funded by STFC grant ST/M000885/1. I. J. R. is supported by STFC Consolidated grant to MSSL ST/N000722/1, and by NERC grants NE/L007495/1, NE/P017150/1, and NE/P017185/1.

References

Agapitov, O., Glassmeier, K.-H., Plaschke, F., Auster, H.-U., Constantinescu, D., Angelopoulos, V., et al. (2009). Surface waves and field line resonances: A THEMIS case study. *Journal of Geophysical Research*, *114*, A00C27. https://doi.org/10.1029/2008JA013553

Archer, M. O., Horbury, T. S., Eastwood, J. P., Weygand, J. M., & Yeoman, T. K. (2013). Magnetospheric response to magnetosheath pressure pulses: A low-pass filter effect. *Journal of Geophysical Research: Space Physics*, *118*, 5454–5466. https://doi.org/10.1002/jgra.50519

Baker, G. J., Donovan, E. F., & Jackel, B. J. (2003). A comprehensive survey of auroral latitude Pc5 pulsation characteristics. *Journal of Geophysical Research*, *108*(A10), 1384. https://doi.org/10.1029/2002JA009801

Barnes, A. (1966). Collisionless damping of hydromagnetic waves. *The Physics of Fluids*, *9*(8), 1483–1495. https://doi.org/10.1063/1.1761882

Berube, D., Sanny, J., Taus, R., & Garoutte, A. (2014). Dayside distribution of Pc5 wave power in the quiet magnetosphere and its response to the solar wind. *Planetary and Space Science*, *97*(Supplement C), 1–8. https://doi.org/10.1016/j.pss.2014.04.012

Brautigam, D. H., & Albert, J. M. (2000). Radial diffusion analysis of outer radiation belt electrons during the October 9, 1990, magnetic storm. *Journal of Geophysical Research*, *105*(A1), 291–309. https://doi.org/10.1029/1999JA900344

Cao, M., McPherron, R. L., & Russell, C. T. (1994). Statistical study of ULF wave occurrence in the dayside magnetosphere. *Journal of Geophysical Research*, *99*(A5), 8731–8753. https://doi.org/10.1029/93JA02905

Chen, L., & Hasegawa, A. (1974). A theory of long-period magnetic pulsations: 1. Steady state excitation of field line resonance. *Journal of Geophysical Research*, *79*(7), 1024–1032. https://doi.org/10.1029/JA079i007p01024

Chi, P. J., Lee, D.-H., & Russell, C. T. (2006). Tamao travel time of sudden impulses and its relationship to ionospheric convection vortices. *Journal of Geophysical Research*, *111*, A08205. https://doi.org/10.1029/2005JA011578

Claudepierre, S. G., Mann, I. R., Takahashi, K., Fennell, J. F., Hudson, M. K., Blake, J. B., et al. (2013). Van Allen Probes observation of localized drift resonance between poloidal mode ultra-low frequency waves and 60 keV electrons. *Geophysical Research Letters*, *40*, 4491–4497. https://doi.org/10.1002/grl.50901

Cowley, S. W. H., & Lockwood, M. (1992). Excitation and decay of solar wind-driven flows in the magnetosphere-ionosphere system. *Annales Geophysicae*, *10*, 103–115.

Degeling, A. W., Ozeke, L. G., Rankin, R., Mann, I. R., & Kabin, K. (2008). Drift resonant generation of peaked relativistic electron distributions by Pc 5 ULF waves. *Journal of Geophysical Research*, *113*, A02208. https://doi.org/10.1029/2007JA012411

Dungey, J. W. (1961). Interplanetary magnetic field and the auroral zones. *Physical Review Letters*, *6*, 47–48. https://doi.org/10.1103/PhysRevLett.6.47

Elkington, S. R. (2013). A review of ULF interactions with radiation belt electrons. In K. Takahashi, et al. (Eds.), *Magnetospheric ULF Waves: Synthesis and New Directions* (pp. 177–193). Washington, DC: American Geophysical Union. https://doi.org/10.1029/169GM12

Elkington, S. R., Hudson, M. K., & Chan, A. A. (1999). Acceleration of relativistic electrons via drift-resonant interaction with toroidal-mode Pc-5 ulf oscillations. *Geophysical Research Letters*, *26*(21), 3273–3276. https://doi.org/10.1029/1999GL003659

Elkington, S. R., Hudson, M. K., & Chan, A. A. (2003). Resonant acceleration and diffusion of outer zone electrons in an asymmetric geomagnetic field. *Journal of Geophysical Research*, *108*(A3), 1116. https://doi.org/10.1029/2001JA009202

Engebretson, M., Glassmeier, K.-H., Stellmacher, M., Hughes, W. J., & Lühr, H. (1998). The dependence of high-latitude Pcs wave power on solar wind velocity and on the phase of high-speed solar wind streams. *Journal of Geophysical Research*, *103*(A11), 26,271–26,283. https://doi.org/10.1029/97JA03143

Fälthammar, C.-G. (1965). Effects of time-dependent electric fields on geomagnetically trapped radiation. *Journal of Geophysical Research*, *70*(11), 2503–2516. https://doi.org/10.1029/JZ070i011p02503

Farrugia, C. J., Elphic, R. C., Southwood, D. J., & Cowley, S. W. H. (1987). Field and flow perturbations outside the reconnected field line region in flux transfer events: Theory. *Planetary Space Science*, *35*, 227–240. https://doi.org/10.1016/0032-0633(87)90091-2

Farrugia, C. J., Gratton, F. T., Bender, L., Biernat, H. K., Erkaev, N. V., Quinn, J. M., et al. (1998). Charts of joint Kelvin-Helmholtz and Rayleigh-Taylor instabilites at the dayside magnetopause for strongly northward interplanetary magnetic field. *Journal of Geophysical Research*, *103*(A4), 6703–6727. https://doi.org/10.1029/97JA03248

Freeman, M. P., & Morley, S. K. (2004). A minimal substorm model that explains the observed statistical distribution of times between substorms. *Geophysical Research Letters*, *31*, L12807. https://doi.org/10.1029/2004GL019989

Geiss, J., Gloeckler, G., & Von Steiger, R. (1995). Origin of the solar wind from composition data. *Space Science Reviews*, *72*(1), 49–60. https://doi.org/10.1007/BF00768753

Gillis, E. J., Rijnbeek, R., Kling, R., Speiser, T. W., & Fritz, T. A. (1987). Do flux transfer events cause long-period micropulsations in the dayside magnetosphere?. *Journal of Geophysical Research*, *92*(A6), 5820–5826. https://doi.org/10.1029/JA092iA06p05820

Glassmeier, K. H., Lester, M., Jedrzejowicz, M., W A, C, Green, C. A., Rostoker, G., et al. (1984). Pc5 pulsations and their possible source mechanisms: A case study. *Journal of Geophysics*, *55*, 109–119.

Gratton, F. T., Farrugia, C. J., & Cowley, S. W. H. (1996). Is the magnetopause Rayleigh-Taylor unstable sometimes? *Journal of Geophysical Research*, *101*(A3), 4929–4937. https://doi.org/10.1029/95JA03064

Hapgood, M. (1992). Space physics coordinate transformations: A user guide. *Planetary and Space Science*, *40*(5), 711–717. https://doi.org/10.1016/0032-0633(92)90012-D

Hartinger, M. D., Turner, D. L., Plaschke, F., Angelopoulos, V., & Singer, H. (2013). The role of transient ion foreshock phenomena in driving Pc5 ULF wave activity. *Journal of Geophysical Research: Space Physics*, *118*, 299–312. https://doi.org/10.1029/2012JA018349

Horne, R. B., Glauert, S. A., Meredith, N. P., Boscher, D., Maget, V., Heynderickx, D., & Pitchford, D. (2013). Space weather impacts on satellites and forecasting the Earth's electron radiation belts with spacecast. *Space Weather*, *11*, 169–186. https://doi.org/10.1002/swe.20023

Hwang, K.-J., & Sibeck, D. G. (2016). Role of low-frequency boundary waves in the dynamics of the dayside magnetopause and the inner magnetosphere. In A. Keiling, D.-H. Lee, & V. Nakariakov (Eds.), *Low-Frequency Waves in Space Plasmas* (pp. 213–239). Hoboken, NJ: John Wiley. https://doi.org/10.1002/9781119055006.ch13

Jian, L., Russell, C. T., Luhmann, J. G., & Skoug, R. M. (2006). Properties of stream interactions at one AU during 1995–2004. *Solar Physics*, *239*(1), 337–392. https://doi.org/10.1007/s11207-006-0132-3

Johnson, N. L., Kotz, S., & Balakrishnan, N. (1994). *Continuous univariate distributions* (Vol. 1, 2nd ed.) New York: Wiley-Interscience.

Kavosi, S., & Raeder, J. (2015). Ubiquity of Kelvin-Helmholtz waves at Earth's magnetopause. *Nature Communications*, *6*, 7019. https://doi.org/10.1038/ncomms8019

Kellerman, A. C., & Shprits, Y. Y. (2012). On the influence of solar wind conditions on the outer-electron radiation belt. *Journal of Geophysical Research*, *117*, A05217. https://doi.org/10.1029/2011JA017253

Kepko, L., & Spence, H. E. (2003). Observations of discrete, global magnetospheric oscillations directly driven by solar wind density variations. *Journal of Geophysical Research*, *108*(A6), 1257. https://doi.org/10.1029/2002JA009676

Kim, K.-H., Cattell, C. A., Lee, D.-H., Takahashi, K., Yumoto, K., Shiokawa, K., et al. (2002). Magnetospheric responses to sudden and quasiperiodic solar wind variations. *Journal of Geophysical Research*, *107*(A11), 1406. https://doi.org/10.1029/2002JA009342

Kivelson, M. G., & Southwood, D. J. (1986). Coupling of global magnetospheric MHD eigenmodes to field line resonances. *Journal of Geophysical Research*, *91*(A4), 4345–4351. https://doi.org/10.1029/JA091iA04p04345

Kivelson, M. G., Etcheto, J., & Trotignon, J. G. (1984). Global compressional oscillations of the terrestrial magnetosphere: The evidence and a model. *Journal of Geophysical Research*, *89*(A11), 9851–9856. https://doi.org/10.1029/JA089iA11p09851

Komar, C. M., & Cassak, P. A. (2016). The local dayside reconnection rate for oblique interplanetary magnetic fields. *Journal of Geophysical Research: Space Physics*, *121*, 5105–5120. https://doi.org/10.1002/2016JA022530

Kuo, H., Russell, C. T., & Le, G. (1995). Statistical studies of flux transfer events. *Journal of Geophysical Research*, *100*(A3), 3513–3519. https://doi.org/10.1029/94JA02498

Li, W., Ma, Q., Thorne, R. M., Bortnik, J., Zhang, X.-J., Li, J., et al. (2016). Radiation belt electron acceleration during the 17 March 2015 geomagnetic storm: Observations and simulations. *Journal of Geophysical Research: Space Physics*, *121*, 5520–5536. https://doi.org/10.1002/2016JA022400

Liu, J., Angelopoulos, V., Sibeck, D., Phan, T., Pu, Z. Y., McFadden, J., et al. (2008). THEMIS observations of the dayside traveling compression region and flows surrounding flux transfer events. *Geophysical Research Letters*, *35*, L17S07. https://doi.org/10.1029/2008GL033673

Liu, W., Sarris, T. E., Li, X., Ergun, R., Angelopoulos, V., Bonnell, J., & Glassmeier, K. H. (2010). Solar wind influence on Pc4 and Pc5 ULF wave activity in the inner magnetosphere. *Journal of Geophysical Research*, *115*, A12201. https://doi.org/10.1029/2010JA015299

Lockwood, M. (1991). Flux transfer events at the dayside magnetopause: Transient reconnection or magnetosheath dynamic pressure pulses? *Journal of Geophysical Research*, *96*(A4), 5497–5509. https://doi.org/10.1029/90JA02389

Lockwood, M., Owens, M. J., Barnard, L. A., Bentley, S., Scott, C. J., & Watt, C. E. (2016). On the origins and timescales of geoeffective IMF. *Space Weather*, *14*, 406–432. https://doi.org/10.1002/2016SW001375

Mann, I. R., Lee, E. A., Claudepierre, S. G., Fennell, J. F., Degeling, A., Rae, I. J., et al. (2013). Discovery of the action of a geophysical synchrotron in the Earth's Van Allen radiation belts. *Nature Communications*, *4*, 2795. https://doi.org/10.1038/ncomms3795

Mann, I. R., Milling, D. K., Rae, I. J., Ozeke, L. G., Kale, A., Kale, Z. C., et al. (2008). The upgraded CARISMA magnetometer array in the THEMIS era. *Space Science Reviews*, *141*, 413–451. https://doi.org/10.1007/s11214-008-9457-6

Mann, I. R., Murphy, K. R., Ozeke, L. G., Rae, I. J., Milling, D. K., Kale, A. A., & Honary, F. F. (2013). The role of ultralow frequency wave in radiation belt dynamics. In D. Summers, et al. (Eds.), *Dynamics of the Earth's Radiation Belts and Inner Magnetosphere* (pp. 69–92). Washington, DC: American Geophysical Union. https://doi.org/10.1029/2012GM001349

Mann, I. R., & Wright, A. N. (1999). Diagnosing the excitation mechanisms of Pc5 magnetospheric flank waveguide modes and FLRs. *Geophysical Research Letters*, *26*(16), 2609–2612. https://doi.org/10.1029/1999GL900573

Mann, I. R., Wright, A. N., Mills, K. J., & Nakariakov, V. M. (1999). Excitation of magnetospheric waveguide modes by magnetosheath flows. *Journal of Geophysical Research*, *104*(A1), 333–353. https://doi.org/10.1029/1998JA900026

Mathie, R. A., & Mann, I. R. (2000). A correlation between extended intervals of ULF wave power and storm-time geosynchronous relativistic electron flux enhancements. *Geophysical Research Letters*, *27*(20), 3261–3264. https://doi.org/10.1029/2000GL003822

Mathie, R. A., & Mann, I. R. (2001). On the solar wind control of Pc5 ULF pulsation power at mid-latitudes: Implications for MeV electron acceleration in the outer radiation belt. *Journal of Geophysical Research*, *106*(A12), 29,783–29,796. https://doi.org/10.1029/2001JA000002

McIlwain, C. E. (1961). Coordinates for mapping the distribution of magnetically trapped particles. *Journal of Geophysical Research*, *66*(11), 3681–3691. https://doi.org/10.1029/JZ066i011p03681

McPherron, R. L. (2005). Magnetic pulsations: Their sources and relation to solar wind and geomagnetic activity. *Surveys in Geophysics*, *26*(5), 545–592. https://doi.org/10.1007/s10712-005-1758-7

Menk, F. W. (2011). Magnetospheric ULF waves: A review. In W. Liu & M. Fujimoto (Eds.), *The Dynamic Magnetosphere. IAGA Special Sopron Book Series* (Vol. 3, pp. 223–256). Dordrecht: Springer. https://doi.org/10.1007/978-94-007-0501-2_13

Mishin, V. V. (1993). Accelerated motions of the magnetopause as a trigger of the Kelvin-Helmholtz instability. *Journal of Geophysical Research*, *98*(A12), 21,365–21,371. https://doi.org/10.1029/93JA00417

Murphy, K. R., Mann, I. R., & Sibeck, D. G. (2015). On the dependence of storm time ULF wave power on magnetopause location: Impacts for ULF wave radial diffusion. *Geophysical Research Letters*, *42*, 9676–9684. https://doi.org/10.1002/2015GL066592

Nakagawa, T., Nishida, A., & Saito, T. (1989). Planar magnetic structures in the solar wind. *Journal of Geophysical Research*, *94*(A9), 11,761–11,775. https://doi.org/10.1029/JA094iA09p11761

National Semiconductor Corporation (1980). Power spectra estimation, Application Note 255, National Semiconductor Corporation.

Newbury, J. A., Russell, C. T., Phillips, J. L., & Gary, S. P. (1998). Electron temperature in the ambient solar wind: Typical properties and a lower bound at 1 AU. *Journal of Geophysical Research*, *103*(A5), 9553–9566. https://doi.org/10.1029/98JA00067

Obayashi, T., & Jacobs, J. A. (1958). Geomagnetic pulsations and the Earth's outer atmosphere. *Geophysical Journal of the Royal Astronomical Society*, *1*(1), 53–63. https://doi.org/10.1111/j.1365-246X.1958.tb00034.x

Otto, A., Lee, L. C., & Ma, Z. W. (1995). Magnetic field and plasma properties associated with pressure pulses and magnetic reconnection at the dayside magnetopause. *Journal of Geophysical Research*, *100*(A8), 14,895–14,911. https://doi.org/10.1029/95JA00417

Owens, M., & Cargill, P. (2004). Non-radial solar wind flows induced by the motion of interplanetary coronal mass ejections. *Annales Geophysicae*, *22*(12), 4397–4406. https://doi.org/10.5194/angeo-22-4397-2004

Owens, M. J., & Forsyth, R. J. (2013). The heliospheric magnetic field. *Living Reviews in Solar Physics*, *10*(1), 5. https://doi.org/10.12942/lrsp-2013-5

Owens, M. J., Cargill, P. J., Pagel, C., Siscoe, G. L., & Crooker, N. U. (2005). Characteristic magnetic field and speed properties of interplanetary coronal mass ejections and their sheath regions. *Journal of Geophysical Research*, *110*, A01105. https://doi.org/10.1029/2004JA010814

Owens, M. J., Riley, P., & Horbury, T. S. (2017). Probabilistic solar wind and geomagnetic forecasting using an analogue ensemble or "similar day" approach. *Solar Physics*, *292*(5), 69. https://doi.org/10.1007/s11207-017-1090-7

Ozeke, L. G., Mann, I. R., & Rae, I. J. (2009). Mapping guided Alfvén wave magnetic field amplitudes observed on the ground to equatorial electric field amplitudes in space. *Journal of Geophysical Research*, *114*, A01214. https://doi.org/10.1029/2008JA013041

Ozeke, L. G., Mann, I. R., Murphy, K. R., Rae, I. J., & Milling, D. K. (2014). Analytic expressions for ULF wave radiation belt radial diffusion coefficients. *Journal of Geophysical Research: Space Physics*, *119*, 1587–1605. https://doi.org/10.1002/2013JA019204

Ozeke, L. G., Mann, I. R., Murphy, K. R., Rae, I. J., Milling, D. K., Elkington, S. R., et al. (2012). ULF wave derived radiation belt radial diffusion coefficients. *Journal of Geophysical Research*, *117*, A04222. https://doi.org/10.1029/2011JA017463

Ozeke, L. G., Mann, I. R., Turner, D. L., Murphy, K. R., Degeling, A. W., Rae, I. J., & Milling, D. K. (2014). Modeling cross L shell impacts of magnetopause shadowing and ULF wave radial diffusion in the Van Allen belts. *Geophysical Research Letters*, *41*, 6556–6562. https://doi.org/10.1002/2014GL060787

Pahud, D. M., Rae, I. J., Mann, I. R., Murphy, K. R., & Amalraj, V. (2009). Ground-based Pc5 ULF wave power: Solar wind speed and MLT dependence. *Journal of Atmospheric and Solar-Terrestrial Physics*, *71*(10), 1082–1092. https://doi.org/10.1016/j.jastp.2008.12.004

Paschmann, G., Haerendel, G., Papamastorakis, I., Sckopke, N., Bame, S. J., Gosling, J. T., & Russell, C. T. (1982). Plasma and magnetic field characteristics of magnetic flux transfer events. *Journal of Geophysical Research*, *87*(A4), 2159–2168. https://doi.org/10.1029/JA087iA04p02159

Percival, D., & Walden, A. (1993). *Spectral analysis for physical applications*. Cambridge University Press.

Plunkett, S. P., & Wu, S. T. (2000). Coronal mass ejections (CMES) and their geoeffectiveness. *IEEE Transactions on Plasma Science*, *28*(6), 1807–1817. https://doi.org/10.1109/27.902210

Pokhotelov, D., Rae, I. J., Murphy, K. R., & Mann, I. R. (2015). The influence of solar wind variability on magnetospheric ULF wave power. *Annales Geophysicae*, *33*(6), 697–701. https://doi.org/10.5194/angeo-33-697-2015

Radoski, H. R. (1966). Magnetic toroidal resonances and vibrating field lines. *Journal of Geophysical Research*, *71*(7), 1891–1893. https://doi.org/10.1029/JZ071i007p01891

Rae, I. J., Donovan, E. F., Mann, I. R., Fenrich, F. R., Watt, C. E. J., Milling, D. K., et al. (2005). Evolution and characteristics of global Pc5 ULF waves during a high solar wind speed interval. *Journal of Geophysical Research*, *110*, A12211. https://doi.org/10.1029/2005JA011007

Rae, I. J., Mann, I. R., Murphy, K. R., Ozeke, L. G., Milling, D. K., Chan, A. A., et al. (2012). Ground-based magnetometer determination of in-situ Pc4-5 ULF electric field wave spectra as a function of solar wind speed. *Journal of Geophysical Research*, *117*, A04221. https://doi.org/10.1029/2011JA017335

Reeves, G. D., Morley, S. K., Friedel, R. H. W., Henderson, M. G., Cayton, T. E., Cunningham, G., et al. (2011). On the relationship between relativistic electron flux and solar wind velocity: Paulikas and Blake revisited. *Journal of Geophysical Research*, *116*, A02213. https://doi.org/10.1029/2010JA015735

Rostoker, G., Samson, J. C., Creutzberg, F., Hughes, T. J., McDiarmid, D. R., McNamara, A. G., et al. (1995). CANOPUS—A ground-based instrument array for remote sensing the high latitude ionosphere during the ISTP/GGS prgoram. *Space Science Reviews*, *71*(1), 743–760. https://doi.org/10.1007/BF00751349

Russell, C., Le, G., & Kuo, H. (1996). The occurrence rate of flux transfer events. *Advances in Space Research*, *18*(8), 197–205. https://doi.org/10.1016/0273-1177(95)00965-5

Russell, C. T., & Elphic, R. C. (1978). Initial ISEE magnetometer results: Magnetopause observations. *Space Science Reviews*, *22*(6), 681–715. https://doi.org/10.1007/BF00212619

Russell, C. T., & Elphic, R. C. (1979). ISEE observations of flux transfer events at the dayside magnetopause. *Geophysical Research Letters*, *6*(1), 33–36. https://doi.org/10.1029/GL006i001p00033

Schwartz, S. J., Paschmann, G., Sckopke, N., Bauer, T. M., Dunlop, M., Fazakerley, A. N., & Thomsen, M. F. (2000). Conditions for the formation of hot flow anomalies at Earth's bow shock. *Journal of Geophysical Research*, *105*(A6), 12,639–12,650. https://doi.org/10.1029/1999JA000320

Shue, J.-H., Song, P., Russell, C. T., Steinberg, J. T., Chao, J. K., Zastenker, G., et al. (1998). Magnetopause location under extreme solar wind conditions. *Journal of Geophysical Research*, *103*(A8), 17,691–17,700. https://doi.org/10.1029/98JA01103

Sibeck, D. G. (1990). A model for the transient magnetospheric response to sudden solar wind dynamic pressure variations. *Journal of Geophysical Research*, *95*(A4), 3755–3771. https://doi.org/10.1029/JA095iA04p03755

Simms, L. E., Pilipenko, V. A., & Engebretson, M. J. (2010). Determining the key drivers of magnetospheric Pc5 wave power. *Journal of Geophysical Research*, *115*, A10241. https://doi.org/10.1029/2009JA015025

Song, P., Le, G., & Russell, C. T. (1994). Observational differences between flux transfer events and surface waves at the magnetopause. *Journal of Geophysical Research*, *99*(A2), 2309–2320. https://doi.org/10.1029/93JA02852

Southwood, D. (1974). Some features of field line resonances in the magnetosphere. *Planetary and Space Science*, *22*(3), 483–491. https://doi.org/10.1016/0032-0633(74)90078-6

Spasojevic, M., Shprits, Y. Y., & Orlova, K. (2015). Global empirical models of plasmaspheric hiss using Van Allen Probes. *Journal of Geophysical Research: Space Physics*, *120*, 10,370–10,383. https://doi.org/10.1002/2015JA021803

Stoica, P., & Moses, R. (2005). *Spectral analysis of signals*. Prentice Hall.

Takahashi, K. (2016). ULF waves in the inner magnetosphere. In A. Keiling, D.-H. Lee, & V. Nakariakov (Eds.), *Low-frequency Waves in Space Plasmas* (pp. 51–63). Hoboken, NJ: John Wiley. https://doi.org/10.1002/9781119055006.ch4

Takahashi, K., & Ukhorskiy, A. Y. (2007). Solar wind control of Pc5 pulsation power at geosynchronous orbit. *Journal of Geophysical Research*, *112*, A11205. https://doi.org/10.1029/2007JA012483

Takahashi, K., & Ukhorskiy, A. Y. (2008). Timing analysis of the relationship between solar wind parameters and geosynchronous Pc5 amplitude. *Journal of Geophysical Research*, *113*, A12204. https://doi.org/10.1029/2008JA013327

Takahashi, K., Yumoto, K., Claudepierre, S. G., Sanchez, E. R., Troshichev, O. A., & Janzhura, A. S. (2012). Dependence of the amplitude of Pc5-band magnetic field variations on the solar wind and solar activity. *Journal of Geophysical Research*, *117*, A04207. https://doi.org/10.1029/2011JA017120

Thomson, D. J. (1982). Spectrum estimation and harmonic analysis. *Proceedings of the IEEE*, *70*(9), 1055–1096. https://doi.org/10.1109/PROC.1982.12433

Walker, A. (1981). The Kelvin-Helmholtz instability in the low-latitude boundary layer. *Planetary and Space Science*, *29*(10), 1119–1133. https://doi.org/10.1016/0032-0633(81)90011-8

Walker, A. D. M. (2002). Excitation of field line resonances by MHD waves originating in the solar wind. *Journal of Geophysical Research*, *107*(A12), 1481. https://doi.org/10.1029/2001JA009188

Walker, A. D. M. (2004). *Magnetohydrodynamic waves in geospace: The theory of ULF waves and their interaction with energetic particles in the solar-terrestrial environment*. CRC Press.

Wang, C.-P., Thorne, R., Liu, T. Z., Hartinger, M. D., Nagai, T., Angelopoulos, V., et al. (2017). A multispacecraft event study of Pc5 ultralow-frequency waves in the magnetosphere and their external drivers. *Journal of Geophysical Research: Space Physics*, *122*, 5132–5147. https://doi.org/10.1002/2016JA023610

Wang, Y. L., Elphic, R. C., Lavraud, B., Taylor, M. G. G. T., Birn, J., Russell, C. T., et al. (2006). Dependence of flux transfer events on solar wind conditions from 3 years of Cluster observations. *Journal of Geophysical Research*, *111*, A04224. https://doi.org/10.1029/2005JA011342

Wolfe, A. (1980). Dependence of mid-latitude hydromagnetic energy spectra on solar wind speed and interplanetary magnetic field direction. *Journal of Geophysical Research*, *85*(A11), 5977–5982. https://doi.org/10.1029/JA085iA11p05977

Zong, Q.-G., Zhou, X.-Z., Li, X., Song, P., Fu, S. Y., Baker, D. N., et al. (2007). Ultralow frequency modulation of energetic particles in the dayside magnetosphere. *Geophysical Research Letters*, *34*, L12105. https://doi.org/10.1029/2007GL029915

Erratum

In the originally published version of this article, the Supporting Information as originally published was missing the associated figures. The figures have been reinstated, and the present version may be considered the authoritative version of record.